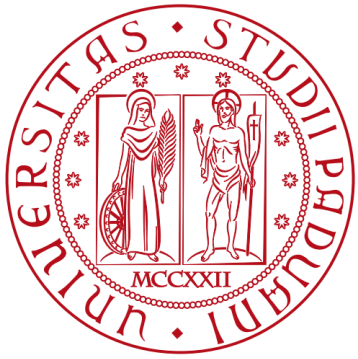

UNIVERSITÀ DEGLI STUDI DI PADOVA

DIPARTIMENTO DI INGEGNERIA INDUSTRIALE

CORSO DI LAUREA MAGISTRALE IN INGEGNERIA CHIMICA E DEI PROCESSI INDUSTRIALI

Tesi di Laurea Magistrale in
Ingegneria Chimica e dei Processi Industriali

DEM Simulations of percolating particles in binary mixtures

Relatore: Prof. Andrea Claudio Santomaso

Correlatore: Dott.ssa Silvia Volpato

Laureando: DARIO BONDI'

ANNO ACCADEMICO 2022 – 2023

Abstract

The aim of the thesis is to study the phenomenon of discharging of binary mixtures of granular material in order to better understand the percolation mechanism, which consists of the relative movement of small particles moving through the void space between the larger ones.

The studied system consists of a silo which is filled with the binary mixture and subsequently discharged in funnel flow. The investigation was conducted using the LIGGGHTS simulator through which it was possible to represent the filling and discharging behavior of the granular material mixtures using DEM approach.

In the first part of the thesis, the percolation phenomenon and the DEM approach are presented; then, will be described the parametric analysis conducted to find the parameters to introduce in DEM simulations. Finally, several simulations were conducted using binary mixtures with different diameter ratios and different compositions.

The data obtained from the simulations were processed and compared with the experimental data in order to validate the results achieved.

Contents

Introduction

Solids, granular materials and powders are widely used in many sectors of the process industries, and several phenomena related to them are widespread in nature.

In fact, many industries are characterized by numerous processes involving solid materials of all kinds and which exploit their chemical and physical properties both as raw materials or as final products; for example, we find them in the food, pharmaceutical, metallurgical, cosmetic, oil and many other industries.

Despite the great importance of processes involving solid materials, such as crystallization, granulation, drying, extrusion and mixing, the studies and development of technologies concerning solid materials have seemed to take second place to those based on liquid and gaseous phases. This is due to the difficulty in describing the complex physics that characterizes granular materials. In recent years, however, there has been greater attention to this type of process, which has been studied more closely.

Usually, these substances are mixtures of granular materials composed of particles with different physical and chemical properties. They are characterized by properties that involve individual particles, such as shape, size and density, and at the same time by properties related to the bulk behavior, such as bulk density, porosity and size distribution (PSD).

The study of this thesis focuses on one of the main mechanisms concerning the characterization of solid mixtures, i.e. the percolation mechanism, in particular the case under consideration is the percolation in binary mixtures of granular materials through the study of the composition of mixtures discharged by a silo. The mixtures of granular materials have a natural tendency to segregate, one of the main mechanisms that cause segregation is percolation, which consists in the relative movement of the small particles in the mixture, which move through the empty space among the bigger ones. In some cases, this phenomenon does not have serious consequences, and it is even wanted, but in fields such as pharmaceuticals or food it can represent an important problem. Just think in the pharmaceutical field of a drug composed of two active ingredients, it is important that each tablet contains the correct composition of both substances. If at the end of the process, the drug was not composed of the correct composition of active ingredients, it would not be suitable for the use for which it was produced, with the risk of causing serious damage to health in extreme cases.

This thesis will expose the main characteristics of the segregation and percolation phenomena. The case of the composition coming out of a silo of binary mixtures of granular material with different starting compositions will then be analyzed. The results obtained in a previous phase in the laboratory will be compared with those obtained through simulations conducted with the DEM method, using LIGGGHTS software. Finally, the obtained results will be presented and commented.

Chapter 1

Mixing and Segregation

In industries, fundamental importance is given to solid mixing processes, especially in sectors where it is necessary to respect the precise composition of the products, such as in the pharmaceutical sector or in the production of detergents; in some cases, in fact, a product with too low active substances would be ineffective, while a product containing too much could even be harmful.

1.1 Mixing mechanisms and types of mixtures

A study conducted by Lacey in 1954 (M. Rhodes, 2008) led to the identification of three main powder mixing mechanisms:

1) **Effect of shear stresses**. Mechanism that derives from shear stresses which, acting on the system, create layered sliding zones; mixing occurs as a result of particle exchange between these layers.
2) **Diffusion**. Mechanism relating to the movement of particles along an inclined plane.
3) **Convection**. Mechanism that consists in the movement of a certain quantity of particles within the mass of the system.

Talking about binary mixtures, three types can be distinguished based on the degree of mixing obtained. First of all, the perfect mixture, which has the same composition of particles regardless of the portion from which a sample is taken. The random mixture, i.e. a mixture whose probability of finding a particle of a component is the same in all positions of the mixture and equal to the proportion of that component considering all the system. Finally, the segregating mixture, in which due to the phenomenon called segregation there is a higher probability of finding a component in a specific zone within the mixture.
Examples of what is meant by perfect, random and segregating mixtures of two components are shown in Figure 1.1.

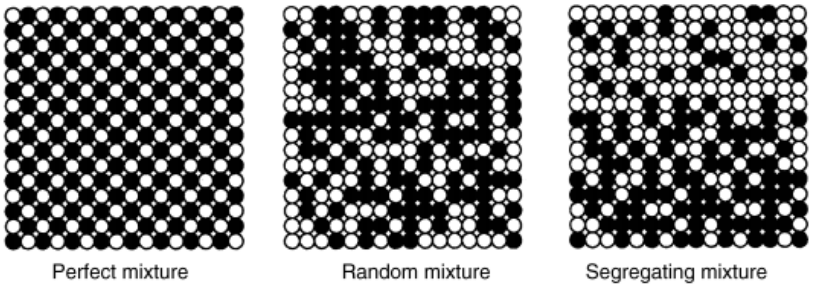

Figure 1.1 – *Sketch of perfect, random and segregating mixtures of two components. (M. Rhodes. Introduction to Particle Technology, 2nd Edition, 2008)*

Actually, it is impossible to obtain a perfect mixture, so the aim is to obtain as far as possible a random mixture. In some cases, it is possible to obtain mixtures with higher quality than random by exploiting the natural attractive forces between the particles; these mixtures are obtained through mixtures called "structured" or "interactive".

Dealing with systems made up of hundreds or thousands of elements, the best approach to use for studying mixing is a statistical one. The key parameter that is used to evaluate the degree of mixing is the variance. The lower the variance value the better the mixing performance, so what is wanted to achieve is to minimize this value as much as possible. Among the models, the first was proposed by Lacey in 1943, who demonstrated that for binary mixtures composed of particles of equal size the standard deviation can be calculated through the following formula:

$$\sigma_R = \sqrt{\frac{\sum(p-\bar{p})^2}{n_o - 1}} \tag{1.1}$$

From which the variance between samples:

$$\sigma_R^2 = \frac{pq}{n_o} \tag{1.2}$$

Where n_o is the total number of particles in the sample, p and q represent the fraction of the two components in the mixture, $\bar{p}$ is the average calculated as $\bar{p} = (p_1 + p_2 \ldots + p_n)/n_o$.

While the variance between samples for a single component in its unmixed state, which corresponds to the worst state in terms of mixing, is:

$$\sigma_o^2 = pq \tag{1.3}$$

Lacey's model on the other hand requires the knowledge of total number of particles that make up the system, which is obviously very difficult, if not even impossible.

In companies and laboratory, it is common practice to weigh the components before mixing them, hence Stange in 1954 proposed to base the calculation of the variance on the weight of the solid phases to be mixed. This allows you to calculate the variance in terms of component weight according to the formula:

$$\sigma_R^2 = \frac{PQ}{M}\left[P\overline{w_Q}\left(1+\frac{\sigma_Q^2}{\overline{w}_Q^2}\right)+Q\overline{w_P}\left(1+\frac{\sigma_P^2}{\overline{w}_P^2}\right)\right] \tag{1.4}$$

Where P and Q are the mass fractions of the two components, M is the mass of the sample taken, σ_P and σ_Q are the standard deviations of the weight distribution and $\overline{w_P}$ and $\overline{w_Q}$ are the mean mass calculated based on the number of particles of the two compounds according to the following formula:

$$\overline{w_P} = \frac{\pi}{6}\rho_s \int_{x-min}^{x-max} x^3\, n_o(x)dx \tag{1.5}$$

Even in this case, however, knowledge of the total number of particles in the system, n_o, is needed. The problem was then overcome with the Poole-Taylor-Wall model of 1964, which is based exclusively on mass distribution. In this case the variance is calculated according to the formula:

$$\sigma_R^2 = \frac{PQ}{M}\left(P\overline{W_Q}+Q\overline{W_P}\right) \tag{1.6}$$

Where $\overline{W_P}$ and $\overline{W_Q}$ are the mean mass calculated based on the weight of the two compounds according to the following formula:

$$\overline{W_P} = \frac{\pi}{6}\rho_s \int_{x-min}^{x-max} x^3\, n_3(x)dx \tag{1.7}$$

Assuming spherical particles and homogeneous density.

In this regard, looking at the plot of logarithm of variance as a function of time, shown in Figure 1.2, it is possible to see that, starting from $\log\sigma_o^2$, there is a sustained and constant decrease over time, until a value of $\log\sigma_R^2$ is reached, which corresponds to the minimum value of the variance, at that point the value of the variance no longer decreases and remains constant. The moment in which this value is reached corresponds to the closest value to perfect mixing.

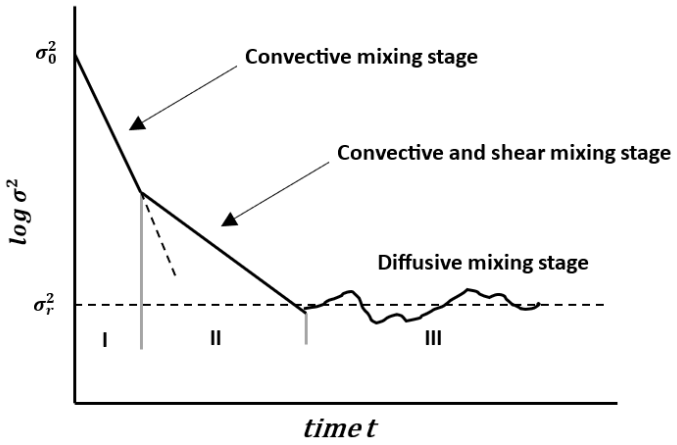

Figure 1.2 - *Plot of logarithm of variance as a function of time.*

Following the plot, it is possible to notice a first area in which the variance strongly decreases, in that section the dominant regime is the convective one. Subsequently the slope decreases, and the zone is characterized by both the convective mechanism and the effect of shear stresses. Finally, when the constant value of the logarithm of the variance is reached, the dominant mechanism is the diffusive one.

As mentioned before, the logarithm of the variance reaches a minimum value which corresponds to the maximum of the mixing, i.e. a situation in which the mixture reaches the maximum level of randomness. On the other hand, the variance does not reach a constant value, but oscillates around that value within a fixed range, i.e. the calculated error. Therefore, the value of the variance must always be considered as $\sigma^2 \pm \text{error}$.

A phenomenon to take into consideration is that in reality, when the powders are filled into the mixing equipment, the filling movement itself produces an initial mixing. This means in practice that the starting value on the logarithm of variance vs time plot, i.e. $\log \sigma_o^2$, starts from a smaller value than the ideal case in which this phenomenon is not considered. This also means that the value of the minimum perfect mixing time is reached much earlier than expected.

The reasons why the variance is considered one of the ideal indices for studying this process is that it is an additive parameter and being a squared value, there is no difference whether the deviation around the mean value is positive or negative.

As seen previously, it is possible to quantitatively evaluate the quality of a mixture using the limits of random variance, σ_R^2, and unmixed mixture variance, σ_o^2, as reference values. However, to understand how close the mixture under examination is to one limit or the other, it

is possible to use an index called the mixing index, M, which represents the relationship between unmixingness and randomness and is defined as:

$$M = \frac{\sigma^2 - \sigma_R^2}{\sigma_o^2 - \sigma_R^2} \tag{1.8}$$

The mixing index can be defined in several ways, so it is always important to specify the definition used.

1.2 Segregation

The best mixing quality, however, is related to a lower degree of segregation.

Segregation is a phenomenon that involves binary mixtures whose components have different properties such as size, density, etc.; these mixtures during movement, pouring, transport or processing are subject to relative movements between the particles with respect to each other, these movements create accumulations of one of the two components in preferential areas with a consequent decrease in the degree of mixing of the system.

Segregation due to size and density results from the effect of several interactions within the system between different particles and/or between particles and walls of the environment; since the preferred state of free-flowing dust is segregation, it is easy to realize how important the study of this phenomenon is.

Among the causes, the difference in size of components is more significant than the density, which is often rather irrelevant, except in the case of gas fluidization in which the difference in density causes important segregation phenomena.

One of the big problems is that segregation can also result from phases after mixing, in fact, even starting from a sufficiently random mixture, it is necessary to pay great attention to the processing and handling phases in order to obtain good product quality. If this were not to be the case, the movements to which the mixtures are subjected would certainly lead to demixing and segregation, with a consequent variation in the bulk density of the product.

1.2.1 Segregation mechanisms

Williams in the 90s identified four mechanisms that lead systems to segregation.

1) **Trajectory segregation**. The velocity of particles during motion depends on their size and density. The distance covered by a particle moving horizontally before stopping, namely the resistance to motion in a fluid, is calculated through Stokes' law, taking into account the density and viscosity of the fluid according to the formula:

$$d = \frac{U\rho_p x^2}{18\mu} \tag{1.9}$$

where U is the velocity of the particle, x the diameter of the particle, ρ_p the density of the particle and μ the viscosity of the fluid.

It is evident that a particle of larger diameter will cover a longer distance before stopping, resulting in segregation of particles with different diameters or densities. In Figure 1.3 is shown a sketch of what has been described.

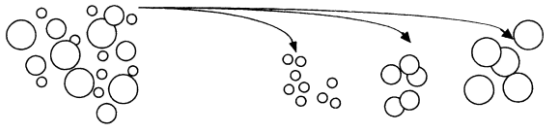

Figure 1.3 – *Sketch of trajectory segregation.*
(M. Rhodes. Introduction to Particle Technology, 2nd Edition, 2008)

2) **Percolation of fine particles**. When a system of particles is perturbed by stresses and movements, a reorganization occurs in the packing of the particles. The spaces that are created allow the particles to move from bottom to top and vice versa. This phenomenon becomes even more common if the particles that make up the mixture have different sizes; in fact, small particles will have greater ease in moving through the spaces created between large particles, finally accumulating in preferential areas it brings to segregation. In general, for liquid or gaseous systems, vibrations or agitation promote the mixing process, but in the case of systems composed of powders or solid particles this leads to segregation.

Segregation by percolation is a phenomenon that often occurs during loading and unloading in granular material storage silos in which, in the case of a funnel flow regime, inclined surfaces are created which act as preferential paths for fine particles

and lead to segregation. In Figure 1.3 is shown a sketch of percolation mechanism of fine particles moving through the gaps created between large particles.

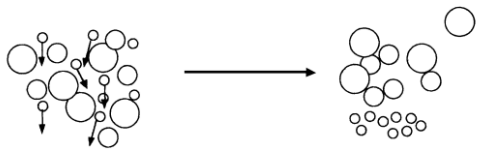

Figure 1.4 – *Sketch of segregation by percolation.*
(M. Rhodes. Introduction to Particle Technology, 2nd Edition, 2008)

3) **Rising of coarse particles due to vibrations**. When a mixture composed of particles of different sizes is subjected to vibrations, a phenomenon which consists in the upward movement of particles with larger diameters occurs. This movement is due to the fact that with vibrations, therefore rhythmic disturbances, small particles move downwards, occupying the area below large particles. Small particles gradually occupy the lower areas of the system, creating a sort of support surface for large particles. This mechanism has been interpreted in terms of the creation and filling of voids under the particles of large size or lower density by the particles of smaller size or higher density.
In 2001 Mobius et al. have focused on the study of the phenomenon and in particular on the rising time, they have demonstrated that the rising tendency of one of the two compounds is related to the density of particles and also the rising tendency is reversed for particles with very low density, which is why it has been hypothesized that there is some other contribution to this phenomenon. Furthermore, they demonstrated that the gaseous medium in which the system is located also contributes to influencing the mechanism. Also Rhodes et al. in 2003 studied the phenomenon, suggesting that it is linked to a sort of floating effect created by pressure gradients during the vibrations to which the system is subject.

4) **Segregation by elutriation**. This mechanism particularly concerns systems such as silos in the filling phase. If the system is composed of a large percentage of fine particles with a diameter lower than 50 microns, air is displaced during the filling of the container, creating resistance to the fall of small particles and causing them to remain in suspension. This leaves time for large particles to occupy the lower area of the container and does not allow the system to remain homogeneous. In fact, once the filling phase is

finished, the system will present preferential areas in which the fine particles are concentrated. Figure 1.4 shows a sketch of what has been described.

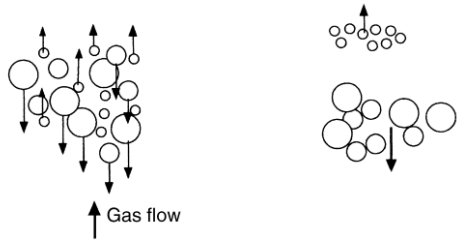

Figure 1.5 – *Sketch of segregation by elutriation.*
(M. Rhodes. Introduction to Particle Technology, 2nd Edition, 2008)

In addition to those proposed by William, there are other mechanisms that cause segregation. As an example, consider a given amount of granular mixture being dropped onto a flat surface. In reference to the topic of this work, consider the process of filling a silo or the material that settles on the underlying surface after discharging; in both cases the material settles creating a heap. The movement make the particles to slide along the inclined surface of the heap; during the sliding, smaller particles are more likely to get trapped in cavities on the surface than larger particles. As a result, smaller particles tend to remain confined in the cavities, while larger particles flow or roll downwards to the base of the accumulation. This phenomenon is known as *sifting*. The greater the difference in size between the particles, the greater the sifting effect.

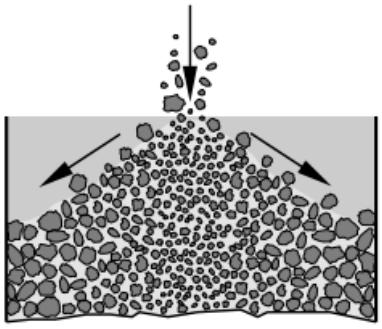

Figure 1.6 - *Segregation by particle size on a heap surface, formed by central filling of a silo, due to the sifting effect. (Schulze, Dietmar. Powders and bulk solids. Springer International Publishing, 2021)*

1.2.2 Segregation in silos

In silos, segregation mechanisms can take place both on the free surface, during filling, and inside the particle bed during discharging.

A characteristic phenomenon throughout the material loading phase consists in the formation of stationary layers at the center of the heap created on the free surface. These become unstable as the thickness increases and intermittently slide downward, as an avalanche does, across the surface of the particle bed (Figure 1.7.a).

Velocity gradients develop within avalanches which lead to shear deformations (Figure 1.7.b). This causes a migration of fine particles towards the lower layers of the avalanche due to percolation.

This mechanism leads to the formation of alternating layers of fine and coarse particles, to which is added the sifting effect described above, resulting in a greater concentration of fine particles in the center of the silo compared to the peripheral areas.

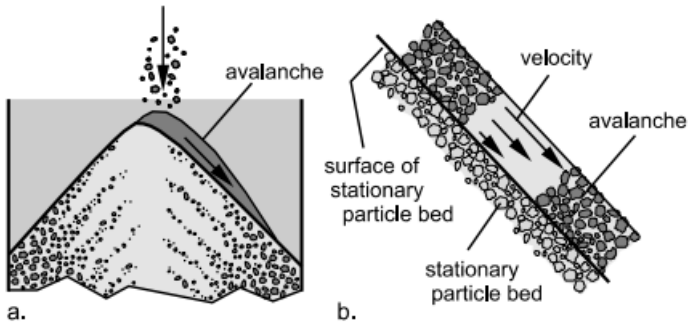

Figure 1.7 - *Segregation on a heap due to percolation and sifting. a) formation of an avalanche; b) velocity gradient and percolation in the avalanche. (Schulze, Dietmar. Powders and bulk solids. Springer International Publishing, 2021)*

As regards the inner part of the particle bed, in silos discharging in a funnel flow regime, the fine particles percolate from the central flow zone towards the stagnant zones; more details on this topic will be presented in chapter §2.

Furthermore, all materials are characterized by a certain angle of repose, i.e. the angle formed by the heap when is placed on a plane with respect to the surface itself. In the case of a mixture, it occurs that the materials with a greater angle of repose will produce a heap with a greater slope on the top, while the materials with a smaller angle of repose will be found further down. Generally, this characteristic is related to the properties of the particles, such as their shape or their capacity to flow.

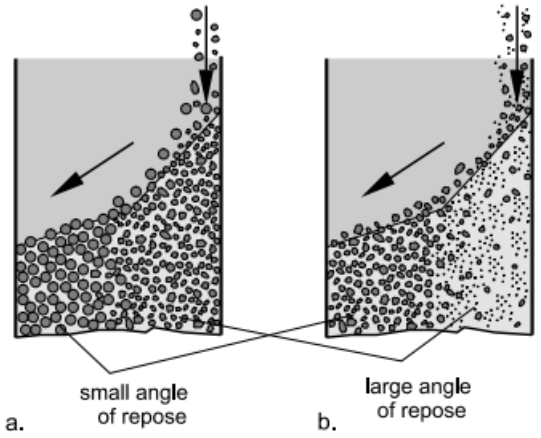

Figure 1.8 - *Segregation due to different angles of repose resulting from particle shape (a) and fines content (b). (Schulze, Dietmar. Powders and bulk solids. Springer International Publishing, 2021)*

The mass flow rate of the material also plays a role in segregation on inclined surfaces because it affects the thickness of the particle layer that falls along the surface.

1.2.3 Segregation reduction

As previously mentioned, among the causes that lead to segregation, the difference in size of the components is more significant than the difference in density. From this it is easy to understand that to reduce segregation it is possible to act by reducing the absolute size of both components.

For systems composed of very small particles, with diameters < 30 microns and densities between 2000 and 3000 kg/m^3, interparticle forces such as electrostatic, capillary and Van der Waals forces are much stronger than gravitational and inertial forces. These attractive forces prevent the particles from moving freely within the system, forming agglomerations between particles of different nature and this decreases the system's tendency to segregate.

Furthermore, the formation of agglomerates leads to a random mixture, where the smaller the particle size, the less the standard deviation of the samples taken and the higher the quality of the mixture.

In other systems, for example those composed of powders with a strong tendency to flow, therefore with very low friction coefficients between the particles, a solution for reducing segregation is the addition of small quantities of liquid. The liquid phase will act as an agglomerant, preventing the particles from moving within the system.

The adhesive nature of some types of granular material can be exploited for the formation of mixtures, which are called ordered or interactive mixtures, of better quality than random ones.

They are composed by fine particles with diameter smaller than 5 microns which naturally have the tendency to adhere to the surface of the larger particles, forming agglomerates. Figure 1.9 shows a sketch of the agglomerations between particles of different nature and size.

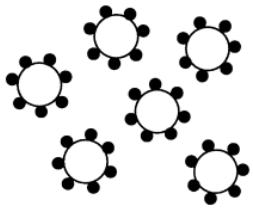

Figure 1.9 - *Sketch of the agglomerations between particles.*
(M. Rhodes. Introduction to Particle Technology, 2nd Edition, 2008)

This technique, which exploits the difference in size and the interparticle attraction forces, is used in industries when very strict standards are needed in terms of mixture quality, for example in pharmaceutical companies.
For processes in which it is not possible to apply these strategies, it is necessary to avoid operations that could promote segregation mechanisms, such as casting or the formation of inclined sliding planes.

1.3 Scale of scrutiny

The quality and the properties of a mixture, intended as the final product of the process, are strictly linked to the purpose for which it was designed. As mentioned previously, based on the use for which the mixture was produced it is necessary to respect standards as precisely as possible. In 1953 Danckwerts introduced the term "scale of scrutiny" which refers to the maximum extension of the segregation zones of a mixture above which it cannot be considered as adequately mixed, of course depending on the type and the purpose for which it was produced.
For example, in the case of a washing powder, the scale of scrutiny refers to the quantity of active ingredients present in each measuring cup taken from the box. The percentage composition in each measuring cup must be the same as that found in the box and must not vary significantly between the first and last taken.
The smaller the scale of scrutiny, the lower the quality of the mixture; decreasing the scale to the limit value leads to the individual particles.

Chapter 2

Silos and discharge regimes

In industries, silos are commonly used for short-term storage (M. Rhodes, 2008) of granular materials. The simplicity and versatility of this equipment, in fact, have made this practice one of the most used and widely spread for the protection and management of powders for thousands of years (M. Rhodes, 2008).
Only after 1964, thanks to the publication of the studies conducted by Jenike, were introduced the criteria that influence the flow of granular material in silos; before that silos were designed without any standards and the construction was based exclusively on hypotheses and experience.
Up to now, several studies have been conducted regarding the structure of the hoppers and the measurement of the materials properties, needed for the correct design of this equipment.

2.1 Mass flow and Funnel flow

Silos are essentially composed of the body called *bunker*, which is divided into *bin*, namely the section with parallel sides, often cylindrical or rectangular, and *hopper*, namely the final truncated cone, or converging part.
During the design phase, it is necessary to take into account the purpose for which they are designed, in order to be easy to use both during the loading phase, but mostly during the discharging phase. What is desired is to have a flow that is controlled and predictable.
When a bulk solid discharges under gravity from a silo, one must distinguish between mass flow and funnel flow:

1) ***Mass flow***, in which the material is discharged following a regular order along the axis of the silo. Here the entire volume of the container is in motion, although not necessarily all at the same speed. This regime is characterized by the fact that the flow channel coincides with the walls of the container. The mass flow is described as “first in, first out” which means that the material that is put into the bin first will be the first that is

discharged. Mass flow is possible only if the hopper walls are steep and/or low enough in friction. If the hopper wall is too flat or too frictional, funnel flow will occur (Schulze, 2008).

2) ***Funnel flow***, in which the tendency for the material to flow and the friction forces between particles, and between particles and silo walls, cause the central region of the silo to discharge first; the granular material follows a preferential path as it encounters less resistance to sliding; subsequently the areas closest to the walls remain unloaded. The mass flow is described with the expression "first in, last out", to indicate that part of the material that is loaded first remains stationary at the walls of the container and will be unloaded only after the central area, composed of the material subsequently loaded, will be emptied.

A sketch of the two flow regimes is shown in Figure 2.1.

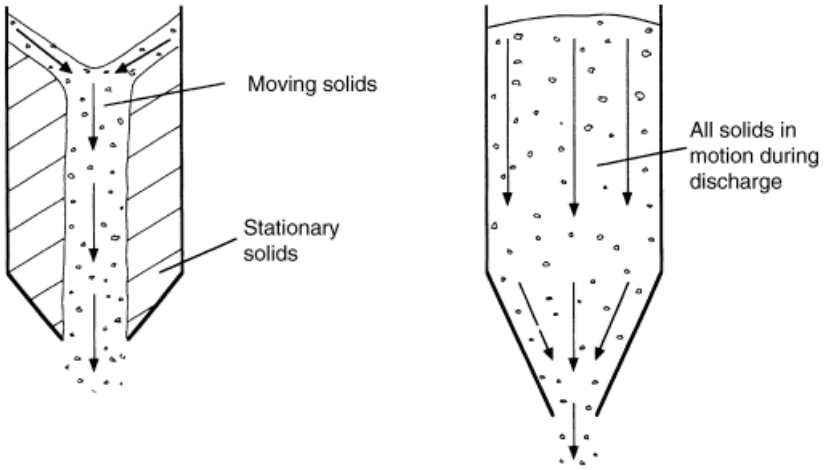

Figure 2.1 – *Sketch of flow regimes: (Left) funnel flow; (Right) mass flow. (M. Rhodes. Introduction to Particle Technology, 2nd Edition, 2008)*

In some cases, it is possible that a third regime arises given by a sort of composition of the two described above, which has characteristics of funnel flow in the bin part and mass flow in the hopper, near the exit; this is called *expanded flow*.

Generally, almost all discharges take place in the mass flow regime, but in some cases, the funnel flow regime is preferred. The choice depends on the nature of the materials contained in

the silos and the advantages and disadvantages of the two regimes. The mass flow regime has the advantage of consisting of a uniform movement involving the entire volume of the container, so it is possible to use steady-state approximations. The mass is not significantly compressed thanks to the low stresses, from this it follows that the bulk density of the discharged powder remains constant and independent of the height of the silos. Since all the mass is discharged in almost regular order, there are no stagnant areas, which prevents the risk that some material remains stuck in the hopper. This problem can arise in the case of a funnel flow regime, in which there is the risk that the residence time is too long, and the material can degrade.

The main disadvantage of the mass flow regime is given by the fact that the flow channel coincides with the walls of the container and in some cases, based on the nature of the content, this leads to strong erosion of the internal wall, which can even lead to powder contamination by the hopper material, for example, metals or plastics. It is clear that this is unacceptable in most cases, just think of food and pharmaceutical production, where contamination is expected to be very low, if not zero. This problem is solved in the funnel flow regime since the areas farther from the center of the silo are unloaded last and the material moves from the bordering areas to the centre following an oblique path.

The funnel flow regime on the other hand is characterized by a strong disadvantage, the oblique movement of the material far from the center of the silo is subject to significant dimensional segregation compared to the mass flow regime.

The last characteristic of the two regimes is related to the height of the silo. In fact, the mass flow regime requires a greater height of the equipment, which also entails a greater height of the room in which it is located; while a silo that discharges in funnel flow requires a lower height. The same reasoning applies to silos that are positioned outside; in fact, the imposing height of some of this equipment creates greater resistance to the wind, so this problem must be taken into consideration and compensated for by structural attention.

From a geometric point of view, to achieve one or the other regime, in conical silos it is necessary to act during the design phase on the diameter of the exit hole and on the inclination angle of the hopper, which depends on the particle-particle and particle-wall friction.

Figures 2.2 (a-d) and 2.3 (a-d) represent the sequence of unloading phases of a section of a silo in the mass flow and funnel flow regime respectively. The alternating color layers are useful for understanding the characteristics of the models described. Note (Figure 2.2) how the surface of the material remains almost flat until it reaches the hopper, while (Figure 2.3) the

characteristic V shape develops (or cone shape, if seen in 3D) typical of the funnel flow regime. Also, note that the areas further down the hopper remain stagnant until the end of the process (Figure 2.3).

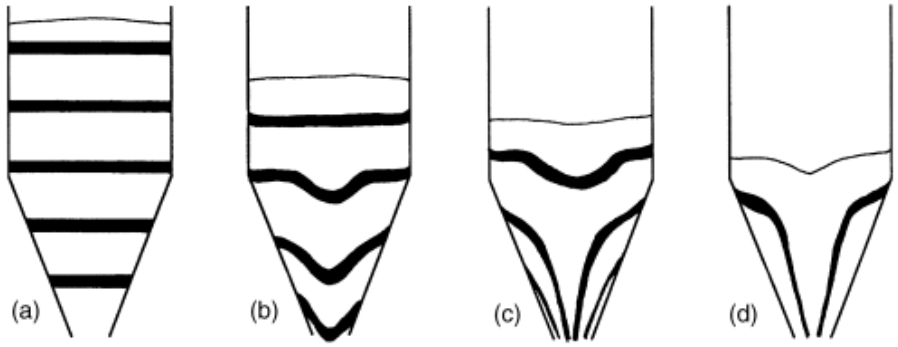

Figure 2.2 – *Sequence of sketches of the discharging process in mass flow regime. (M. Rhodes. Introduction to Particle Technology, 2nd Edition, 2008)*

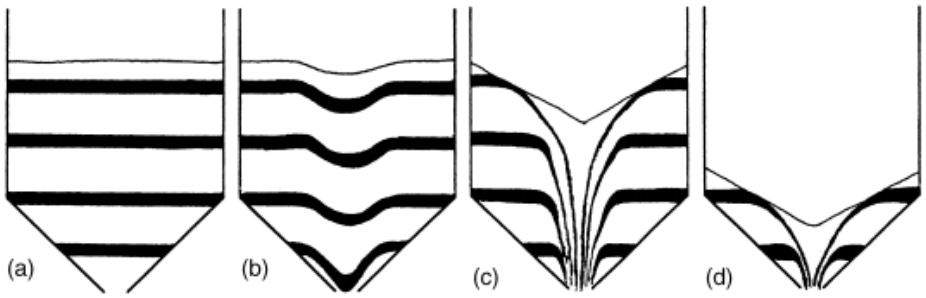

Figure 2.3 - *Sequence of sketches of the discharging process in funnel flow regime. (M. Rhodes. Introduction to Particle Technology, 2nd Edition, 2008)*

When unloading the material, there may be two main problems: 1) the material does not discharge adequately from the exit hole, and 2) the material segregates during unloading.

Problems often occurring during the storage of bulk solids in silos are:

1) **Ratholing or piping**, i.e., the central part of the solid flows, while the stagnant part along the walls is stable enough to remain still without discharging.
2) **Flow is too slow**, i.e., the flow is slow compared to what is required by the process.
3) **No flow due to arching or doming**, i.e., a stable arch of the material is formed in correspondence with the exit hole, and this causes the flow to stop.

4) **Flushing**, i.e., the material is stable enough to form a dome that blocks the flow, but not enough to stop it completely; therefore, unloading occurs only when air manages to enter through the material. What is therefore obtained is that the material is discharged in an irregular way, only if and when the air manages to penetrate and move it.
5) **Incomplete emptying**, i.e., the presence of dead zones inside the cylinder, in which the material remains stationary without being able to be unloaded, even if the rest of the material has been unloaded.
6) **Segregation**, i.e., the flow stops because small particles move through the empty spaces of the larger particles, preventing the possibility of sliding.
7) **Time consolidation**, a phenomenon that occurs in some materials which due to their nature when left still for a certain period of time tend to form stable structures that therefore no longer slide once the hopper is opened. Like table salt or cement.
8) **Caking**, a phenomenon that occurs when some materials in contact with air humidity form stable bonds or bridges, once solidified there is the presence of large particles that cannot flow adequately.

Most of the mentioned problems relate to funnel flow.
To solve these problems, in general, it is necessary to design the hoppers in such a way as to obtain mass flow. To obtain this regime the angle of the cone, with respect to the vertical axis, has to be between 40° and 0°. However, it is not always necessary to have mass flow, there are cases where this is not required.

2.2 Mass flow rate prediction

Since there are many factors that influence the mass flow rate exiting a silo, an exact prediction is rather complicated, if not impossible. Furthermore, many variables are difficult to calculate, and the only option is to rely on assumptions.
Up to now, formulas found in the literature have been derived from experimental observations. Considering a generic silo of diameter, D, and height, H, equipped with an exit hole at the base of diameter, B, as shown in Figure 2.4; it has been observed that the flow rate of granular material exiting the orifice is independent of the filling height, for $H \gg 2B$, and similarly is independent of the bin diameter, for D$\gg 2B$.

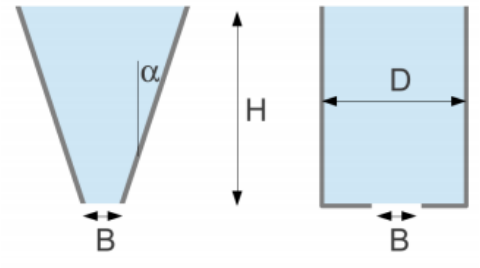

Figure 2.4 – *Sketch of generic silo with symbols.*

The parameters that influence the mass flow rate are, however, bulk density, ρ_b, gravitational acceleration, g, orifice diameter, B, and friction coefficient, μ.

$$W = f(\rho_b, g, B, \mu) \tag{2.1}$$

Since the friction coefficient is dimensionless, carrying out a dimensional analysis the relation has to be of the type:

$$W = C\ \rho_b \sqrt{g}\ B^{5/2} \tag{2.2}$$

Where C is a function of the friction coefficient.

Studies have shown that by plotting the results in the form ln (W) vs ln (B), the slope of the line does not correspond to 5/2, but is a value closer to 3 (more precisely, a value equal to 2.96 has been accepted); furthermore, it was suggested to consider a weak dependence on the filling height, so the correlation becomes:

$$W = C'\ \rho_b \sqrt{g}\ B^{2.69}\ H^{0.04} \tag{2.3}$$

Subsequently, Beverloo et al. (1961), considering the dependence of the flow rate on $B^{5/2}$ to be more correct, plotted their results in the form $W^{2/5}$ vs B (Figure 2.5).

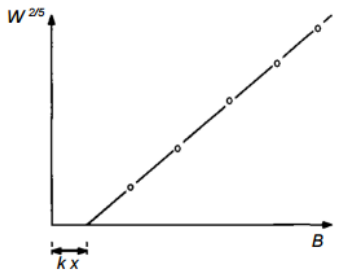

Figura 2.5 – *Plot $W^{2/5}$ vs B as recommended by Beverloo (Beverloo, 1961).*

They observed that the straight line does not intersect the origin but the x-axis at a point proportional to the diameter of the particles, x.

This phenomenon has been attributed to the fact that during discharging the cross section of the exiting material flow is actually smaller than the exit diameter (Schulze, 2008). Therefore, a term equal to kx is subtracted from the diameter of the orifice, B; the correlation then becomes:

$$W = C\,\rho_b\,\sqrt{g}\,(B - kx)^{5/2} \tag{2.4}$$

Where C no longer seems to be a function of μ and has a constant value of 0.58 (in some cases the value of 0.64 is attributed to particular types of soft particles such as spherical glass beads). While k has a constant value of 1.5 for spherical particles, it can also be slightly higher for angular particles.

However, flow prediction calculated through the Beverloo correlation has a range of applicability. In fact, it has been seen that this is valid only for particles whose diameter does not exceed one-sixth of the diameter of the orifice. Particles with larger diameters would increase the risk of forming stable arc structures which would cause blockage of the material (see paragraph §2.3). On the other hand, if the diameter was too small (as a rule of thumb: $x < 400$ μm) the material would suffer from friction with the air, reducing the mass flow rate.

Based on these observations, Beverloo can be applied in the range $B/6 > x > 400$ μm.

Furthermore, the Beverloo correlation is valid only for non-cohesive and almost spherical materials, in silos that discharge in funnel flow (Nedderman, 1992). In the case of cylindrical hoppers discharging in the mass flow regime, the contribution of the inclination angle with respect to the vertical, α, also becomes important. The inclination is considered through the factor k_α (Tanaka and Rose, 1956):

$$\begin{cases} k_\alpha = (\tan\alpha)^{-0.35} & for\ \alpha < 45° \\ k_\alpha = 1 & for\ \alpha \geq 45° \end{cases} \tag{2.5}$$

Finally, the correct correlation is expressed as:

$$W = 0.58\,\rho_b\,\sqrt{g}\,(B - kx)^{5/2}\,k_\alpha \tag{2.6}$$

2.3 Formation stable arches

One of the most frequent and serious problems that occurs using silos is the interruption of the flow through the discharge orifice. What may seem like a minor problem is actually the cause of numerous production stops.

During the design phase it is necessary to pay due attention so that the discharge flow remains constant; to do this it is necessary that the hopper has a sufficiently steep angle and that the opening is sufficiently large with respect to the diameter of particles.

A phenomenon that can lead to the interruption of the correct discharging process consists in the formation of stable structures at the exit hole. These structures can derive from the cohesive nature of some types of material or be the result of a series of forces that lead to the formation of stable arches, with the risk that the flow is interrupted or becomes intermittent.

To avoid this phenomenon, where possible, the entire set of forces involved in the process must be taken into consideration and action must be taken right from the design stage to ensure that the flow has sufficient strength to break this stable structure if it were to form. Figure 2.6 shows a scheme of what has been described, in which a dome of material of thickness Δh forms a stable arch structure in correspondence with the exit hole of diameter B.

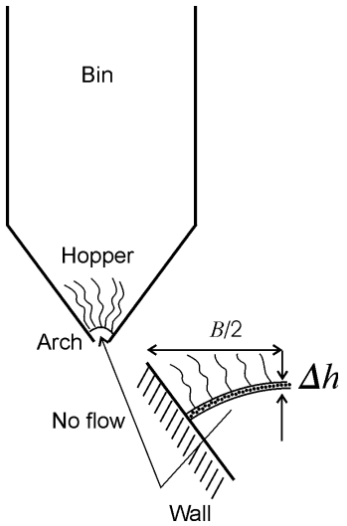

Figure 2.6 - *Stable arc structures formed above the hopper outlet.*

(R. Holdich, Fundamentals of Particle Technology)

Chapter 3

Materials and methods

The aim of this paper is to investigate the segregation mechanisms that occur in devices used for the storage of granular materials through the comparison between experimental data and those obtained from simulations carried out with a DEM approach. The first part of the investigation, therefore, takes place in the laboratory.

For the experimental data, reference was made to the experiments conducted by Prof. A. Santomaso and Dr. Eng. S.Volpato at the ATPLab (Advanced Particle Technology Laboratory) at the industrial engineering department of the University of Padua.

3.1 Materials

The material used in the experiments is a mixture of grains of pasta and couscous with irregular shapes (Figure 3.1). The mixture of the two components (pasta and couscous) allowed a broad particle size distribution ranging from 0.850 mm to 4 mm. The raw material was hence subdivided by sieving into 6 classes: A = 0.850-1 mm, B = 1-1.41 mm, C = 1.41-2 mm, D = 2-2.83 mm, E = 2.83-3.36 mm, F = 3.36-4 mm.

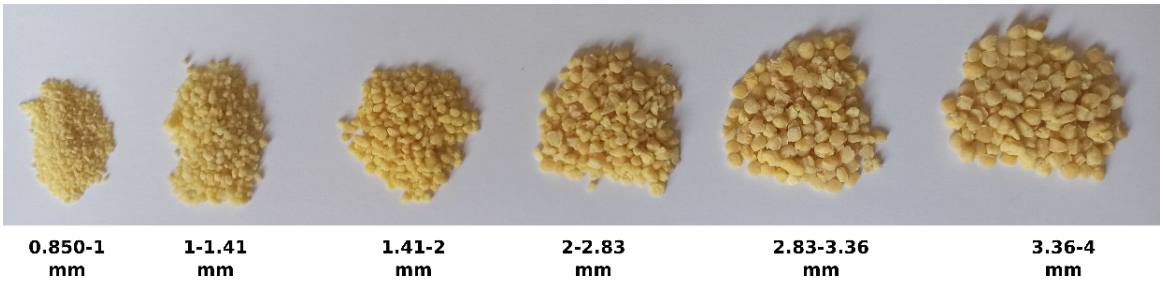

Figure 3.1 - *Photograph of different sized granular material according to PSD obtained by sifting.*

To determine the binary mixtures used in the experiments, two classes were chosen to form the groups of material called fines and coarse. For the first set of experiments the fine group was composed of particles with sieve diameters between 1.41 and 2 mm (d_{f1}= 1.7 mm) and the coarse group was composed of particles with sieve diameters between 3.36 and 4 mm (d_c= 3.68 mm). For the second set of experiments, the coarse group remained equal to that used in

experiment 1, while the fine group was composed of particles with dimensions between 1 and 1.4 mm (d_{f2}= 1.2 mm). Hence, in the first experiment, the particle diameter ratio ($DR = d_c/d_f$) was equal to 2.16; in the second, the diameter ratio was equal to 3.

3.2 Methods

The silo used for the experiments was a silo of a diameter equal to 0.15 m with an inclined hopper (35° to the vertical) as shown in Figure 3.2. The outlet size was unique and equal to 0.029 m. The wall steepness does not guarantee the funnel flow (but mass flow). For this reason, the walls of the hopper were covered with sandpaper (P400). In fact, according to Jenike's theory (Schulze, 2021), increasing the hopper wall friction angle makes it possible to convert a mass flow into a funnel flow. The funnel flow discharge guarantees the segregation of particles during the unloading.

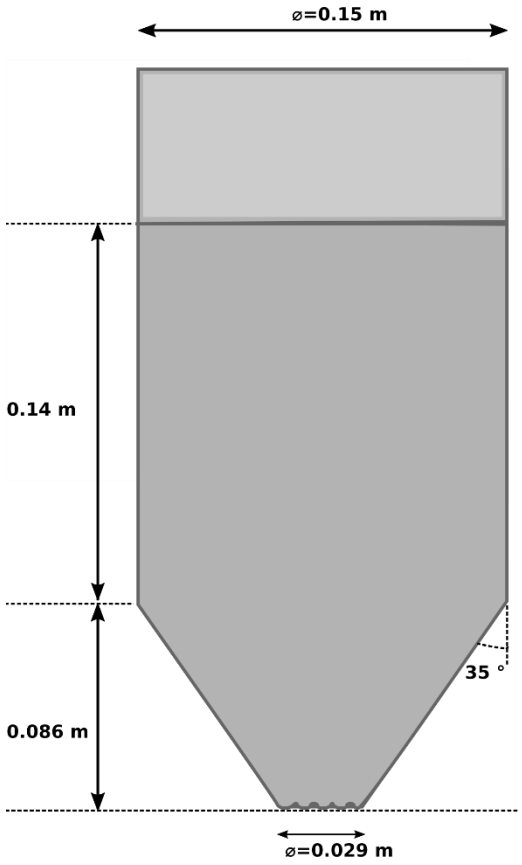

Figure 3.2 – *Sketch of the silo used for the experiment.*

3.2.1 Measure of the discharge rate of the binary mixtures

The discharge rates of different mixtures were measured. For every of the two considered size ratios (DR = 3 and DR = 2.16), eleven mixtures were created ranging the fraction of fine particles inside the mixtures between 0 and 1 ($0 < x_f < 1$), with step 0.1.

Then the silo was filled with about 1700 g of mixture. 100 g batches of binary mixture samples were prepared individually by manual mixing. Each batch was then placed into the silo as successive layers.

Considerable caution was exercised when gently lowering each batch of material onto the upper surface of the bed, using a short pipe section as assistance. This approach is thought to have effectively minimized the potential for segregation caused by particle impacts on the exposed surface during the filling.

To determine the discharge rate, the mass unloaded as a function of time was determined by using a high capacity and resolution electronic balance (RADWAG, PS 6000.R2) that records the incremental value of the discharged mass in the time.

Four repetitions of the same measure (discharged mass vs. time) were done for every mixture. The mass flowrate for every measure was calculated as the slope of the straight line obtained reporting in the x-axis the time and in the y-axis the discharged mass as it is possible to see in Figure 3.3.

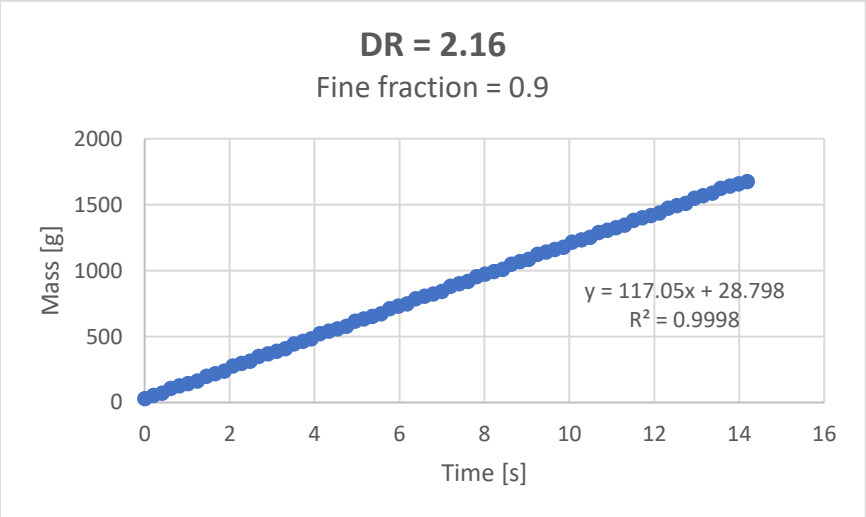

Figure 3.3 – *Mass vs time discharge plot of binary mixture with fine fraction of 0.9 and DR = 2.16*

The mass flow rate as a function of the fines fraction inside the mixture for the two diameter ratios is reported in Figure 3.4.

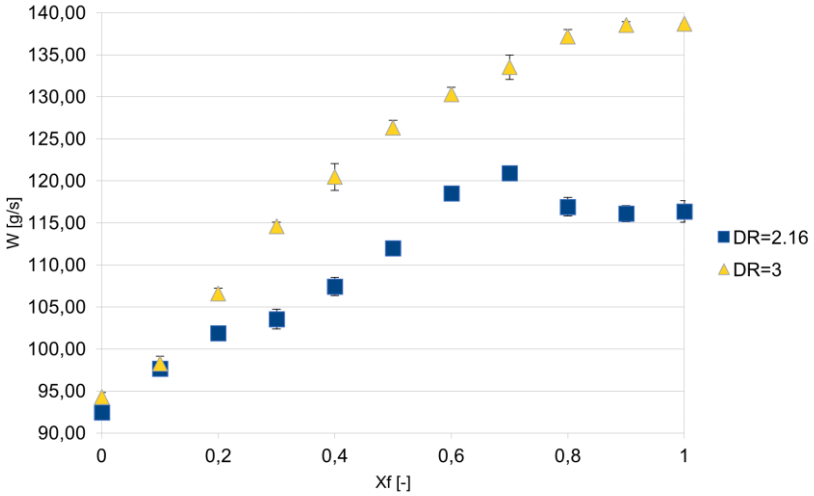

Figure 3.4 - *Mass flow rate as a function of the fines fraction inside the mixture for the two diameter ratios.*

3.2.2 Measure of the bulk porosity of the mixtures

Average static densities of the mixtures ρ_b, were calculated by weighting the mixture in the container with known geometrical volume. The filling of the container was done using a silo that worked in mass-flow regime. The ratio between the mass of the material inside the container after the filling and the volume of the container resulted in the mixture bulk density. The measure was done for the two different size ratios (DR = 2.16 and DR = 3) and mass fraction of fine between 0 and 100%.

Through the intrinsic density value ρ_s, it was possible to calculate the porosity value ε of the different mixtures:

$$\varepsilon = 1 - \frac{\rho_b}{\rho_s} \tag{3.1}$$

In Figure 3.5 the porosity for the two size ratios is reported as a function of the content of fines fraction in the mixtures.

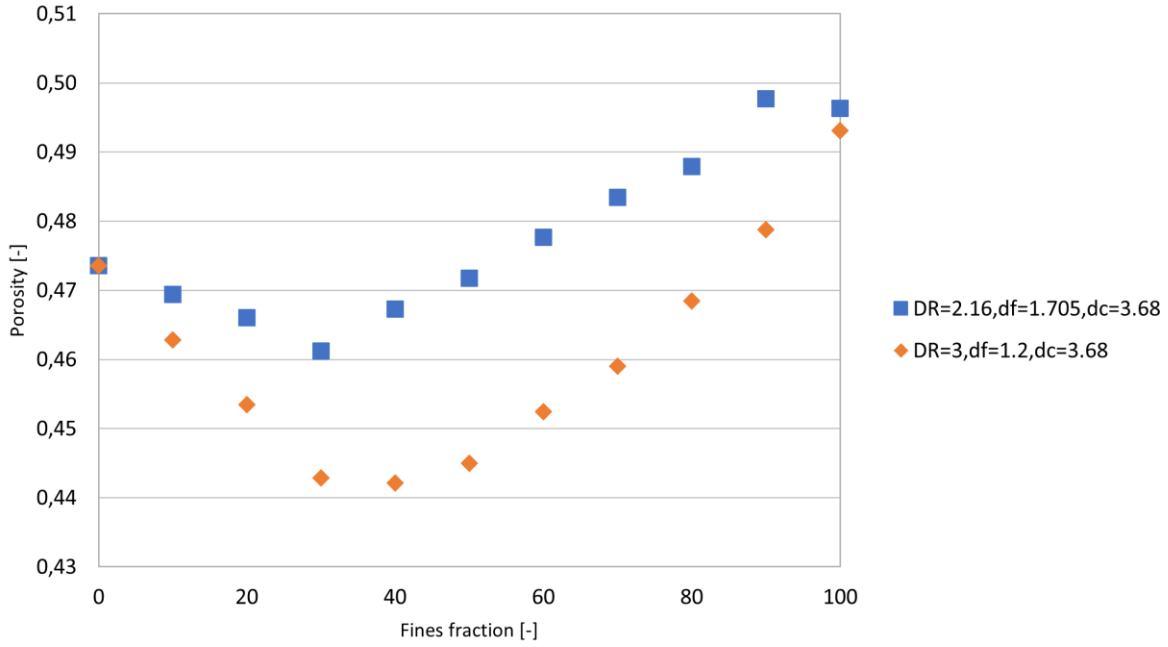

Figure 3.5 - *Porosity as a function of fines fraction in the mixtures for the two size ratios.*

3.2.3 Measure of the segregation during the unloading of silo

The experiments to evaluate the extent of the segregation during the discharge of the silo were conducted for eight mixtures. For every of the two size ratios, DR=3 and DR=2.16, four mixtures were realized with these fractions of fines: 10%, 30%, 50% and 65%. Above this quantity, it is plausible to consider that segregation is practically non-existent, hence no experiments were conducted with mixtures containing fines in quantities above 65% (Arteaga and Tuzun, 1990).

Arteaga and Tuzuz proposed a simple equation to determine the quantity of fine materials in the mixture that makes segregation tend to zero during discharge as a function of the diameter ratio characterizing the binary mixture:

$$\Phi_{F,lim} = \frac{4}{4 + DR} \tag{3.2}$$

For DR = 3, the limit fines fraction is equal to 0.57; for DR = 2.16 the limit fines fraction is equal to 0.65.

The silo was filled with the same amount of mixture for all the experiments and closed with a magnetic cup; then it was vertically placed on a trolley with the discharge outlet facing downward. A graded strip of paper was extended on the floor of the laboratory and fixed with adhesive tape. A second magnet was fixed on the floor at the beginning of the paper strip. When the trolley with the silo passed over the magnet on the floor, the closing cap was automatically detached from the silo outlet allowing the powder mixture to be discharged. During the unloading, the trolley was manually driven along the graded paper strip at constant speed until complete discharge. In this way, a controlled discharge of the powder, at a constant mass flow rate, was obtained. The distance between the silo outlet and the floor was kept constant at 5 cm during the discharge; the velocity with which the silo was moved guarantees the gravity unloading, well described by the Beverloo equation (Arteaga and Tuzun, 1990). All the material was collected and weighed to know the amount of mass discharge; furthermore, at regular sampling distance (100 mm), a sample of material was collected, weighted and screened to obtain the weight fraction. The procedure of discharge and sampling is sketched in Figure 3.6.

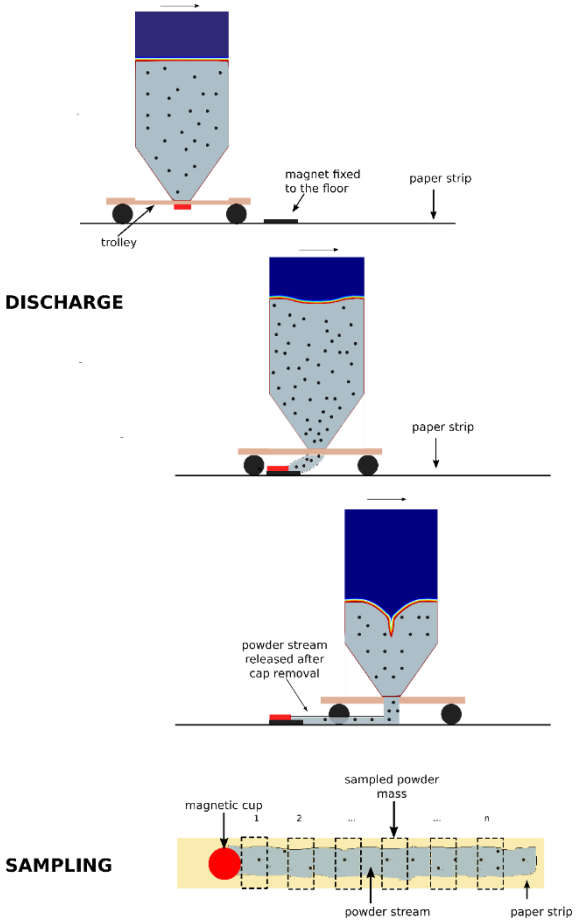

Figure 3.6 – *Sketch of procedure of discharge and sampling*

The segregation of fine particles during the discharge under funnel-flow conditions was monitored by measuring the mass fraction of fine and coarse particles present in the discharged samples, collected at regular intervals, as reported in Figure 3.7. The x-axis of these plots reports the fine mass fraction ϕ_F normalized by the average mass fraction of the initial filling $\phi_{F,0}$. A value greater than 1 indicates segregation of fine material inside the mixture due to percolation of the fine within the hopper. A value lower than 1 suggests the retention of fine materials inside the hopper. A value equal to 1 indicates that no segregation occurs inside the mixture. The y-axis instead reports the cumulative overall mass discharged normalized by the initial total mass loaded into the silo.

The normalized fines mass fraction shows for every DR and every $\phi_{F,0}$ three regions: an initial region where the mass fraction is always greater than 1, an intermediate region where the normalized fines mass fraction is lower than 1 (which indicates retention of fines inside the bulk material remained in the silo) and a final short zone where the normalized fines mass fraction comes back greater than 1.

For DR = 2.16 the extent of segregation is greatest for $\phi_{F,0}$= 0.1. For $\phi_{F,0}$= 0.3, 0.5, 0.65 the intermediate and the final stages show a similar behavior, while the extent of segregation is similar in the initial stage for $\phi_{F,0}$= 0.5, 0.65. However, the extent of segregation is very close to 1 for $\phi_{F,0}$ > 0.3.

Using a greater diameter ratio, DR = 3, which means more difference between the size of fine and the coarse particles that compose the binary mixture, it is possible to appreciate a larger discrepancy in the extent of segregation varying $\phi_{F,0}$. In this case the normalized fines mass fraction is near to 1 for $\phi_{F,0} \geq 0.5$.

Hence, observing these data set, we can assert that the fines segregation tends to stop at lower values of $\phi_{F,0}$ for DR = 2.16 respect to the case DR = 3.

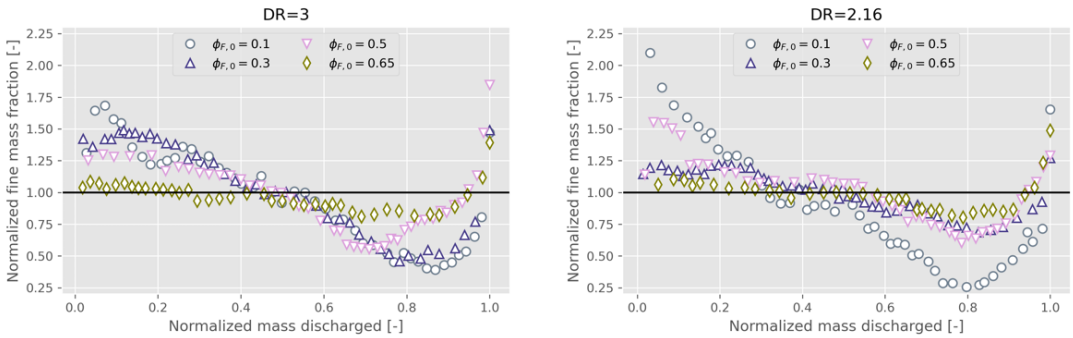

Figure 3.7 – *Normalized fines mass fraction during discharge of a binary mixture from a funnel flow silo at different initial fines mass fraction and two different sizes ratios: DR=3 (left) and DR=2.16 (right).*

Chapter 4

The DEM approach

4.1 Introduction

The microscopic dynamics of the macroscopic behavior of particulate material (Herrmann, 1997; Kishino, 2001; Hinrichsen et al., 2004) is the subject of important studies in which theory and experiments are used together to understand the complex mechanisms involved. Given the complexity of these systems and the enormous number of elements that constitute them, the approach used consists of particle modelling through the so-called Discrete Element Methods (DEM).

The DEM method is made up of the entire set of properties and interaction laws between particles, often also defined as molecular dynamics (MD), which leads to the description of the collective behavior of the dissipative system composed of a large number of particles.

Through this description, it is possible to create simulations for the determination of several properties, such as the pressure of the system as a function of density, or the position and velocity of each particle at any instant of time.

The equations of state obtained, which link the different quantities of the system, allow a macroscopic description of the granular material, which is seen as a complex non-Newtonian compressible fluid (Luding et al., 2001b), including the fluid-solid phase transition.

The criteria and equations on which the so-called molecular dynamics of soft spheres (MD=DEM) are based will be discussed below. That is a simple approach for solving the equations of motion for a system composed of numerous particles that interact with each other and with the walls of the container in which they are placed (Allen et al., 1987; Rapaport, 1995). Both normal and tangential interactions, such as friction, for spherical particles will be discussed.

4.2 The system

The elementary units consist of grains of mesoscopic size that deform under stress. Since representing deformations in a detailed and realistic way is extremely complex, a relationship is established between interaction force and overlap, δ, between two particles, as illustrated in Figure 4.1.

It is important to note that calculating interaction forces based on superposition alone may not adequately account for the non-uniform stress distribution within the particles. Consequently, the results that follow are equivalent to simplified assumptions regarding the correlation between strength and overlap.

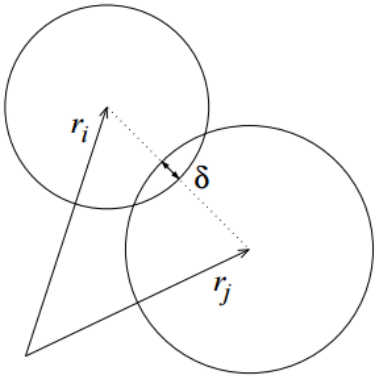

Figura 4.1 – *Two particles contact with overlap δ. (S. Luding, Introduction to Discrete Element Methods, 2008)*

4.3 Equation of motion

The forces acting on a particle can have different nature, we distinguish the interaction forces between particles, between particle and the walls of the system and the external forces applied. Knowing all the forces, f_i, acting on the particles, the problem is reduced to the integration of Newton's laws of motion for the translational and rotational degrees of freedom:

$$m_i \frac{d^2}{dt^2} r_i = f_i + m_i g \tag{4.1}$$

where m_i is the mass of particle i, r_i is the position, fi is the total force calculated as the sum of all the forces, f_i^c, due to contacts with other particles or with walls and g is the gravitational acceleration.

And:

$$I_i \frac{d}{dt}\omega_i = t_i \tag{4.2}$$

Where I_i is the moment of inertia for spherical particles, ω_i the angular velocity, t_i the torsional moment calculated as $t_i = \sum_c (l_i^c \times f_i^c + q_i^c)$, in which q_i^c are torques/couples at contacts other than due to a tangential force, e.g., due to rolling and torsion.

Therefore, a system composed of $D + D(D-1)/2$ differential equations is obtained (with D number of dimensions), easily solvable with a numerical integration tool.

Short-range interactions, typical of this type of systems, allow further optimizations to be used through alternative methods or the use of connected cells. Long-range interactions (such as Coulomb interactions between charged particles), however, do not allow the use of such methods, so they must be considered advanced methods, which will not be covered in this text.

4.4 Normal contact force laws

4.4.1 Linear normal contact model

Considering two spherical particles i and j, of radius a_i and a_j respectively, these interact by meeting each other so that their superposition, defined as:

$$\delta = (a_i + a_j) - (r_i - r_j) \cdot n \tag{4.3}$$

is positive ($\delta > 0$), with unit vector $n = n_{ij} = (r_i - r_j)/|r_i - r_j|$ which points from j towards i.

The force due to contact c applied by particle j on particle i is composed of normal contribution f^n and tangential contribution f^t, so it holds true that:

$$f^c \coloneqq f_i^c = f^n n + f^t t \tag{4.4}$$

The contribution given by the normal contact force is in turn expressed as the sum of two contributions according to the following formula:

$$f^n = k\delta + \gamma_0 v_n \tag{4.5}$$

where $k\delta$ expresses the linear repulsive force, with k spring stiffness, and $\gamma_0 v_n$ expresses the linear dissipative force, with γ_0 viscous damping coefficient and v_n relative velocity in the normal direction calculated as $v_n = -v_{ij} \cdot n = -(v_i - v_j) \cdot n = \delta$.

The model described is called *linear spring-dashpot* and considers the contact between particles as a damped harmonic oscillator. The contact time is expressed as:

$$t_c = \frac{\pi}{\omega}, \quad with\ \omega = \sqrt{(k/m_{12}) - \eta_0^2} \tag{4.6}$$

Where ω is the contact frequency, η_0 is the rescaled damping coefficient calculated as $\eta_0 = \gamma_0/(2m_{ij})$ and m_{ij} is the reduced mass expressed as $m_{ij} = m_i m_j/(m_i + m_j)$.

The contact time has a practical technical importance, in fact, the integration of the equations of motion is stable only if the integration time step, Δt_{DEM}, is much smaller than t_c. For an excessively damped spring, t_c can take on very large values, so it is common practice to use dissipation that is neither too weak nor too strong.

The coefficient of restitution is defined as the ratio between the velocity before and after the collision and is calculated as:

$$r = -v_n'/v_n = exp(-\pi\eta_0/\omega) = exp(-\eta_0 t_c) \tag{4.7}$$

4.4.2. Adhesive, elasto-plastic normal contact model

An alternative method is a variant of the *linear hysteretic spring method* (Walton et al., 1986; Luding, 1998; Tomas, 2000; Luding, 2008a). This is a simplified model that takes into account some nonlinear hysteretic force laws and the possibility that plastic deformations may occur.

The hysteretic repulsive force is expressed as:

$$f^{hys} = \begin{cases} k_1\delta & for\ loading, & if & k_2^*(\delta - \delta_0) \geq k_1\delta \\ k_2^*(\delta - \delta_0) & for\ un/reloading, & if & k_1\delta > k_2^*(\delta - \delta_0) > -k_c\delta \\ -k_c\delta & for\ unloading, & if & -k_c\delta \geq k_2^*(\delta - \delta_0) \end{cases} \tag{4.8}$$

with $k_1 \leq k_2^*$, where k_1 and k_2^* are the slopes of the lines as shown in Figure 4.2.

During contact the force increases proportionally to the overlap δ, up to the maximum overlap δ_{max}. The straight line with slope k_1 corresponds to the maximum possible force for a given δ. Once the maximum overlap is reached, the force decreases from δ_{max} to zero, which corresponds to the value $\delta_0 = (1 - k_1/k_2^*)\delta_{max}$ on the straight line with slope k_2^*. For each possible new contact, the force increases along this line up to its maximum value; if δ increases again, the force follows the straight line with slope k_1 again and δ_{max} must be adjusted accordingly.

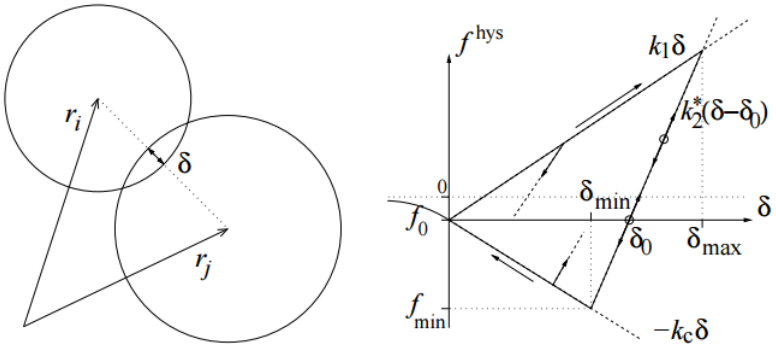

Figure 4.2 - *(Left) two particles contact with overlap δ. (Right) schematic graph of the piecewise linear, hysteretic, adhesive force-displacement model used below (S. Luding, Introduction to Discrete Element Methods, 2008)*

If the overlap decreases below δ_0, there would be negative attractive forces that correspond to the points of the line $-k_c\delta_{min}$ with overlap $\delta_{min} = (k_2^* - k_1)\delta_{max}/(k_2^* + k_c)$.

The value of the minimum force, which corresponds to maximum attraction, is obtained as a function of the parameters k_1, k_2, k_c and δ_{max}.

A further separation would lead to attractive forces $f^{hys} = -k_c\delta$ on the line with slope $-k_c$. Given k_1 and k_2, the maximum attractive force would be for $k_c \to \infty$, so $f_{max}^{hys} = -(k_2 - k_1)\delta_{max}$. Since this would lead to a discontinuity at $\delta = 0$, a finite k_c value is used.

The lines with slope k_1 and $-k_c$ correspond to the range of possible values of the force, only in the case of unloading and reloading does the force take on different values and follows the line with slope k_2.

In Figure 4.2 there are small circles on the line with slope k_2^* which indicate the possible equilibrium states. The first at δ_0 corresponds to a tension-free state and the second, higher up, corresponds to a pre-stressed state.

Although the model just presented would be more realistic, there is no detailed experimental information to support it, so it is preferable to use the linear model.

A further improvement could be achieved by using a value of k_2^* as a function of maximum overlap to represent large and small plastic deformations for strong and weak contact forces, respectively.

A model has recently been developed (Luding et al., 2005; Luding, 2008a) in which the parameter $k_2^*(\delta_{max})$ increases from k_1 to k_2 with maximum overlap until reaching a new parameter denoted as δ_{max}^*.

Therefore, we have that:

$$k_2^*(\delta_{max}) = \begin{cases} k_2 & if \ \ \delta_{max} \geq \delta_{max}^* \\ k_1 + (k_2 - k_1)\delta_{max}/\delta_{max}^* & if \ \ \delta_{max} < \delta_{max}^* \end{cases} \quad (4.9)$$

Furthermore, in this model, in collisions with large deformations the dissipation is caused by the force law of a hysteretic nature, while for small deformations greater dissipations are obtained by considering the normal force as the sum of the hysteretic contribution and the viscous dissipative contribution (which depends on the velocity), so that is $f^n = f^{hys} + \gamma_0 v_n$. The hysteretic model coincides with the linear model if $k_1 = k_2 = k$.

4.4.3. Long range normal forces

Alternatively, medium-range Van der Waals forces can be considered, for which the normal force will be given by the sum of this contribution added to the contribution of the hysteretic forces, such that $f^n = f_i^{hys} + f_i^{VdW}$. These forces are represented through the attractive contribution of the Jennard-Jones potential, as:

$$f^{VdW} = -6(\varepsilon/r_0)\left[\left(r_0/r_{ij}\right)^7 - (r_0/r_c)^7\right] \ \ for \ \ r_{ij} \leq r_c \quad (4.10)$$

where ε is the energy scale, r_0 is the distance to which corresponds the minimum of the potential energy, r_c is the limit distance, r_{ij} is the distance between the particles.

Short-range interactions methods can be applied to medium-range interactions as long as r_c is much larger than the particle diameter.

4.4. Tangential forces

For the contribution due to tangential forces, three different mechanisms can be distinguished:

1. **Sliding friction**

   The relative tangential velocity at the contact points for static and kinetic friction is defined as:

   $$v_t = v_{ij} - n\left(n \cdot v_{ij}\right) \quad (4.11)$$

   While, for the total relative velocity of the surfaces of the particle at contact the following holds true:

   $$v_{ij} = v_i - v_j + a_i' n \times \omega_i + a_j' n \times \omega_j \quad (4.12)$$

Further on, in paragraph §4.5, a method will be shown for calculating the tangential forces acting on the particles in contact starting from the accumulated sliding of the contact points.

The reasons that lead two particles to rotate together are mainly due to rotation of the reference system or non-central collision. The angular rotation velocity is given by the sum of a normal contribution and a tangential contribution $\omega_0 = \omega_0^n + \omega_0^t$. The tangential component is expressed as:

$$\omega_0^t = \frac{n \times (v_i - v_j)}{a_i' + a_j'} \tag{4.13}$$

and is a function of the relative velocity, while the normal component, ω_0^n, is not. Substituting $\omega_i = \omega_j = \omega_0^t$ in the Equation (4.12) we obtain that the equations reported are objective, since the sliding velocity is zero. From this it can be concluded that tangential forces and torques are applied only if the particles rotate with respect to the common rotating reference system.

According to the action and reaction principle, the tangential forces have the same magnitude, but opposite sign, so that $f_j^t = -f_i^t$, while the tangential couples $q_i^{friction} = -a_i' n \times f_i$ and $q_j^{friction} = (a_j'/a_i') q_i^{friction}$ will certainly be parallel, but they could have different magnitude.

The forces and torques together conserve the total angular momentum around the center of mass of the pair, L_{ij}, defined as:

$$L_{ij} = L_i + L_j + m_i r_{i\mathrm{cm}}^2 \omega_0^t + m_j r_{j\mathrm{cm}}^2 \omega_0^t \tag{4.14}$$

Where L_i and L_j are the relative rotational contributions to the particles, $r_{i\mathrm{cm}}$ and $r_{j\mathrm{cm}}$ are the relative distances between the centers of the particles at the center of mass calculated as $r_{\mathrm{cm}} = (m_i r_i + m_j r_j)/(m_i + m_j)$ (Luding, 1998).

The variation of the angular momentum is expressed as the sum of two contributions, the first linked to the variation of the rotation of the particles with respect to their own axis, the second to the variation of the angular momentum of the two masses that rotate around the common center of mass, that is:

$$\frac{dL_{ij}}{dt} = q_i^{friction}\left(1 + \frac{a_j'}{a_i'}\right) + \left(m_i r_{i\mathrm{cm}}^2 + m_j r_{j\mathrm{cm}}^2\right)\frac{d\omega_0^t}{dt} \tag{4.15}$$

Both contributions participate, but cancel each other out, since:

$$q_i^{friction}\left(1+\frac{a_j'}{a_i'}\right)=-\left(a_i'+a_j'\right)n\times f_i=-\left(m_i r_{i\mathrm{cm}}^2+m_j r_{j\mathrm{cm}}^2\right)\frac{d\omega_0^t}{dt} \tag{4.16}$$

2. Rolling friction

In analogy with the sliding velocity, the rolling velocity, v_r^0, is defined as:

$$v_r^0=-a_i' n\times\omega_i+a_j' n\times\omega_j \tag{4.17}$$

This expression, on the other hand, does not guarantee that v_r^0 is objective in general. The rolling velocity has the meaning of quantifying the distance at which the two surfaces of the particles rotate on each other without sliding, so the above expression would be objective only in cases where the particles have equal dimensions or for a particle rolling on a stationary flat surface.

To solve the problem, the reduced radius $a_{ij}'=a_i'a_j'/\left(a_i'+a_j'\right)$ is used, so that the rolling velocity, v_r, can be expressed as:

$$v_r=-a_{ij}'\left(n\times\omega_i-n\times\omega_j\right) \tag{4.18}$$

valid for both particles; furthermore, it is an objective definition since any common rotation cancels out.

As an effect, torques are generated which act as a reaction to rolling. These pairs will have the same magnitude but opposite direction, i.e.:

$$q_i^{rolling}=-q_j^{rolling}=a_{ij}n\times f_r \tag{4.19}$$

where f_r is defined as a *quasi-force*, equal for both particles and not acting on the centers of mass, so the total translational and angular momenta are conserved. The calculation of f_r as a function of rolling velocity will be shown below, in analogy to the friction force.

3. Torsion friction

Relative rotation along the normal direction is defined as:

$$v_0=a_{ij}'\left(n\cdot\omega_i-n\cdot\omega_j\right)n \tag{4.20}$$

note that the reduced radius is also used in this case.

Because of this velocity, torques are generated only when the two particles rotate in the opposite direction and with the parallel axes directed in the normal direction.

Torsion does not cause a common rotation of the particles around the normal direction $n \cdot \omega_0 = n \cdot (\omega_i + \omega_j)/2$ and this makes torsion friction objective.

The torques that are generated have the same magnitude and opposite direction, that is:

$$q_i^{torsion} = -q_j^{torsion} = a_{ij} \times f_o \tag{4.20}$$

Where f_o is the quasi-force, independent of the translational moment. Also in this case, as mentioned for rolling, the torques conserve the total angular momentum. The calculation of the quasi-force, f_o, as a function of the torsion velocity will be shown below.

4.5. The tangential force- and torque-models

To determine f_t, f_r and f_o, we rely on v_t, v_r and v_o respectively using the same procedure but different parameters. The difference, as mentioned previously, is that friction generates a force on the tangential plane by varying both translational and angular momentum, while rolling and torsional resistance generate quasi-forces on the tangential plane and in the normal direction respectively, varying only the angular momentum of the particles.

The procedure that can be used to determine the resistance to sliding, rolling or torsion is shown below. Only the model for sliding friction will be reported as an example, subsequently just the differences in the procedures for the other two resistances will be presented.

4.5.1. Sliding friction model

The Coulomb force gives the relationship between the tangential force and the normal force, that is:

$$f^t < f_C^s \coloneqq \mu^s f^n \tag{4.21}$$

Where μ^s is the coefficient of static friction.

For the sliding case, reference is made to dynamic friction, for which the following applies:

$$f^t = f_C^s \coloneqq \mu^d f^n \tag{4.22}$$

With μ^d dynamic friction coefficient, for which the relation $\mu^d \leq \mu^s$ generally holds.

In the case of static friction, it is necessary for the force to be balanced by a reaction, i.e. by a non-zero tangential force that maintains the static equilibrium.

For a repulsive contact force, so $f^n > 0$, the tangential force is active. In this model the reference value is no longer the force equal to zero, but is an adhesive force; therefore, there will no longer be only f^n, but is taken into consideration the attractive contribution along $-k_c\delta$; so we will have $f^n + k_c\delta$.

If the force is active, the reference system could be rotated with respect to the last time-step, so the tangential reaction is projected (or rather rotated) onto the current tangential plane. The process is iterative, so the tangential spring is described as:

$$\xi = \xi' - n(n \cdot \xi') \tag{4.23}$$

Where ξ' is the spring at the previous iteration, with $|\xi| = |\xi'|$ applied by scaling or rotation. Initially the spring starts from a value of zero, but from the first iteration it acquires a well-defined value. This variation is calculated starting from a test tangential force, given by the sum of the contribution due to the tangential reaction and the contribution of a tangential viscous force, in analogy with the normal viscous force, according to the following formula:

$$f_0^t = -k_t\xi - \gamma_t v_t \tag{4.24}$$

where k_t is the spring stiffness and γ_t is the tangential dissipation parameter.

For $|f_0^t| \leq f_C^s$, with $f_C^s = \mu^s(f^n + k_c\delta)$, there is static friction. As soon as $|f_0^t| > f_C^s$ there will be sliding friction. If it returns to a condition where $|f_0^t| < f_C^d$ it would have static friction again.

Below the Coulomb limit (static friction), the tangential spring is increased, so we have:

$$\xi' = \xi + v_t \Delta t_{MD} \tag{4.25}$$

expression that is used in the next iteration, in Equation (4.23), furthermore in the Equation (4.24) $f^t = f_0^t$ is used.

Above the limit, however, the spring is adjusted to a length consistent with the Coulomb condition, so:

$$\xi' = -\frac{1}{k_t}\left(f_C^d t + \gamma_t v_t\right) \tag{4.26}$$

Where t is the tangential vector, defined as $t = f_0^t / |f_0^t|$.

Inserting this expression into the Equation (4.24) in the next iteration will give $f_0^t \approx f_C^d t$.

The directions of f_0^t and v_t can also have different directions, but the mapping of the Equation (4.26) always works, rotating the new spring to keep the direction of the friction force unchanged and limiting the length according to the Coulomb's law.

The tangential contact law is, therefore, expressed as:

$$f^t = f^t t = +min(f_C, |f_0^t|)t \tag{4.27}$$

The torque due to friction forces at this contact acting on a particle will be equal to:

$$q^{friction} = l_i^c \times f_i^c \tag{4.28}$$

Where l_i^c is the branch vector, connecting the center of the particle with the contact point. The torque acting on the other particle in contact will also be subject to a torque, with the same direction, but generally different magnitude, since l_i^c does not necessarily have the same value. The friction law has four parameters, namely the tangential stiffness (k_t), the static friction coefficient (μ_s), the dynamic friction ratio ($\phi_d = \mu_d/\mu_s$), and the tangential viscosity (γ_t). If the parameters are within the limits, the tangential force is identical to the classic Cundall-Strack spring.
The model, definitions and mappings in the tangential direction can be used in both 3D and 2D.

4.5.2. Rolling resistance model

Three parameters are used for rolling resistance: rolling stiffness (k_r), static rolling friction coefficient (μ_r) and rolling viscosity (γ_r); furthermore, $\phi_r = \phi_d$ is used for the friction law.
In this case the rolling velocity, v_r, is used instead of v_t and the quasi-force f_r is used to calculate the torques, $q^{rolling}$, on the particles.

4.5.3. Torsion resistance model

Three parameters are used for rolling resistance: torsional stiffness (k_o), static torsional friction coefficient (μ_o) and torsional viscosity (γ_o); furthermore, $\phi_o = \phi_d$ is used for the friction law.
In this case the torsion velocity, v_o, is used instead of v_t and the quasi-force f_o is used to calculate the torques, $q^{torsion}$, on the particles.
Here the projection is made along the normal unit vector, not in the tangential plane as for the other two models.

4.6. Background friction

Contact between two particles produces viscous dissipation. In the bulk, where a large number of particles are in contact with each other, this effect is not very efficient due to the long-wavelength cooperative modes of motion (Luding et al., 1994b; Luding et al., 1994a).
Introducing additional damping with the background, the total force acting on particle i is expressed as:

$$f_i = \sum_j (f^n n + f^t t) - \gamma_b v_i \tag{4.28}$$

and the total torque will be:

$$q_i = \sum_j \left(q^{friction} + q^{rolling} + q^{torsion}\right) - \gamma_{br} a_i^2 \omega_i \tag{4.29}$$

In this sense, artificially enhanced damping is understood as the sequence of a rapid relaxation phase followed by an equilibrium phase.
The two equations just reported take into account all the molecules j in contact with the particle i, but the background dissipation can also depend on the medium in which the system is located. The effect of γ_b and γ_{br} must be checked for each parameter group; in fact, it must be small to exclude excessive artificial damping.

4.7. Conclusion

What has been presented is a summary of the main criteria underlying the molecular dynamics of soft particles (MD), defined in engineering through the discrete element method (DEM), which has proven to be a useful tool for the representation and understanding of many granular systems.
Over the years, much attention has been paid to this topic, which has led to the development of predictive models capable of describing and quantifying the complex mechanisms of granular materials.
Further studies are necessary for an even deeper understanding of the topic, which will involve advanced kinetic theories for the description of dense collisional flows and constitutive models for quasi-static dense systems.

Chapter 5

What LIGGGHTS is and how it works

To study the percolation mechanisms during the discharge of a binary mixture from a silo, several simulations were conducted with the DEM approach. Therefore, relying on a simulator known for its high efficiency was of crucial importance for the purpose of this investigation.
In this chapter, first of all, the software with which the simulations were conducted will be presented; subsequently, as an example, extracts of the code used for one of the main simulations carried out will be reported and commented on.

5.1 Introduction

For all simulations, a software called LIGGGHTS was used. This is open-source software for particle simulation using the discrete element method (DEM), distributed by DCS Computing GmbH, based in Linz, Austria. The acronym LIGGGHTS stands for "LAMMPS Improved for General Granular and Granular Heat Transfer Simulations". LAMMPS is a well-known molecular dynamics simulator, widely used in the field of molecular dynamics. Thanks to physical similarities and shared algorithms, LAMMPS offers basic functionality for DEM simulations. The goal of LIGGGHTS is to improve these capabilities, directing them towards industrial applications. Currently, LIGGGHTS is employed by several research institutions around the world. A considerable number of leading companies operating in the chemical, consumer goods, pharmaceutical, agricultural engineering, food manufacturing, steel, mining and plastics manufacturing industries use LIGGGHTS to optimize their manufacturing processes. This software is highly efficient on desktop or laptop computers with single processors but was designed to take full advantage of the potential of parallel computers. It runs on any parallel device that supports C++ compilation and the MPI message passing library, including distributed or shared memory parallel systems. LIGGGHTS is capable of modelling systems with a variable number of particles, which can range from a few units to millions or billions. Furthermore, it is designed to be easily customizable and extendable with new features, such as force fields, atom types, boundary conditions or diagnostics.

LIGGGHTS constitutes an essential component of the CFDEM project, focused on the creation of a new, highly advanced CFD-DEM platform. This tool has remarkable capabilities for modelling a wide range of materials, including soft, solid, and coarse-grained granular materials. LIGGGHTS is suitable for use in particle simulation on a scale ranging from micro to macro, demonstrating great versatility.

The implemented DEM methods allow simulating large granular particles, and LAMMPS provides both linear and nonlinear granular potentials for this purpose. LIGGGHTS further expands these LAMMPS-based capabilities by introducing several new features:

- It is possible to import complex geometry directly from computer-aided design (CAD) into a LIGGGHTS simulation.
- Torque style parameters, such as stiffness and damping coefficient, can be linked to material properties, allowing them to be derived from experimental laboratory data such as density, Young's modulus, Poisson's ratio and coefficient of restitution.
- LIGGGHTS offers the ability to model macroscopic cohesion.
- A dynamic load balancing feature is included.
- Allows import of complex wall geometries directly from CAD.
- Contact force formulation includes options for cohesive forces and rolling friction.
- The particle insertion process has been significantly improved, based on a procedure that uses surface and volume meshes.

It should be emphasized that all features, rules and commands present in LAMMPS are fully compatible with LIGGGHTS.

Unlike some commercial software, LIGGGHTS does not have a graphical user interface. Instead, the user manages the simulation process by composing a text-based input file containing a set of commands to conduct the simulation. This input file is read in sequential order, so the order of the instructions is crucial.

Note that there are two main categories of statements within the LIGGGHTS input file: single commands and corrections. Individual commands are used to establish basic settings for the simulation. Corrections, on the other hand, allows to configure particular aspects of the simulation.

A typical input script for LIGGGHTS is generally divided into four main parts:

1) **Initialization**
   This section is dedicated to defining the parameters that must be configured before creating the particles.
2) **Configuration**
   Here the properties of the material, the characteristics of the particles, the geometry and the generation of the particles themselves are specified.
3) **Detailed Settings**
   In this part detailed settings regarding velocity, memory usage, output options, and so on are defined.
4) **Execution**
   The actual simulation is started through the use of a specific command directly from the computer terminal.

5.2 The present case

For the case in question, the discharge of a binary mixture of granular material from a silo, the simulations were developed in two phases: filling and discharge.
Below, as an example, the main characteristics of the scripts used for the simulation of a binary mixture of 2.46 kg, composed of coarse particles with a diameter of 3.68 mm and fine particles with a diameter of 1.22 mm, ratio between diameters DR=3, with a weight percentage composition of 65% fine and 35% coarse. The scripts of the other simulations will not be reported, they differ only in the above variables, while the geometry and other parameters are the same.

5.2.1 Filling

The script used for the loading phase follows the sequence of the four parts described above.
In the initialization part, the materials were first of all listed, to indicate that throughout the script the coarse particles will be indicated with the number 1, the fine particles with the number 2 and the silo walls with the number 3. Then the variables relating to the particles, such as the

mixture mass, radii, mole fractions, and density, that make up the system were described. Furthermore, Young's modulus, Poisson's ratio and the coefficient of restitution were defined, that are all parameters common to both groups of particles.

```
### INITIALIZATION
# Materials: 1) large particles, 2) small particles, 3) silo walls
# Variables
variable radius1 equal 0.00184 #[m]
variable radius2 equal 0.000613 #[m]
variable nradii equal 2
variable frac1 equal 0.35 #35% large
variable frac2 equal 0.65 #65% fine
variable density equal 1348 #[kg/m3]
variable massP equal 2.46263 #[kg]

variable youngsModulus equal 2.5e7 [MPa]
variable poissonsRatio equal 0.25
variable coefficientRestitution equal 0.5
```

Subsequently, the friction coefficients were defined. For the present case were considered the contributions of sliding friction, indicated by *Friction*, and rolling friction, indicated by *RollingFriction*. It was necessary to define the system through a 3x3 matrix, to distinguish the friction forces based on the type of material in contact. The elements of the matrix therefore represent the friction coefficients between coarse particles (pp11), between fine particles (pp22), between fine and coarse particles (pp12 and pp21) and between fine or coarse particles and the walls (pw13, pw23, wp31 and wp32), lastly, for completeness of the matrix, the friction coefficient between wall and wall (ww33) which has no real physical meaning for the system under examination. The matrix is symmetric, so the elements below the diagonal correspond specularly to those above.

```
# pp11 pp12 pw13
# pp21 pp22 pw23
# wp31 wp32 ww33

variable pp11Friction equal 0.4
variable pp12Friction equal 0.4
variable pw13Friction equal 0.4
variable pp22Friction equal 0.4
variable pw23Friction equal 0.4
variable ww33Friction equal 0.4

variable pp11RollingFriction equal 0.3
variable pp12RollingFriction equal 0.7
variable pw13RollingFriction equal 0.6
variable pp22RollingFriction equal 0.7
variable pw23RollingFriction equal 0.9
variable ww33RollingFriction equal 0.6
```

The time step variable is defined to indicate that each iteration corresponds to 0.00001 seconds.

```
variable deltaT equal 0.00001 #[s]
```

Below have been defined the variables relating to the system geometry domain.

```
variable rsilo equal 0.1/2

# Geometies
variable xlo equal -0.075
variable xhi equal 0.075
variable ylo equal -0.075
variable yhi equal 0.075
variable zlo equal -0.086403
variable zhi equal 0.2165

# Declare domain
region      domain block -0.075 0.075 -0.075 0.075 -0.086403 0.30
units box
create_box  3 domain

# Neighbor listing
neighbor    0.003 bin
neigh_modify      delay 0
```

Accompanied by some preliminary information, for example are indicated the units of measurement, the type of material and the boundary domain.

```
# Preliminaries
units       si
atom_style  granular
atom_modify       map array
boundary    f f f
newton            off
communicate       single vel yes
#processors 1 2 2
```

In the setup phase, the program provides information on the system to be simulated based on the variables written during the initialization phase.

```
### SETUP

# Material and interaction properties required
fix m1 all property/global youngsModulus peratomtype
${youngsModulus} ${youngsModulus} ${youngsModulus}
fix m2 all property/global poissonsRatio peratomtype
${poissonsRatio} ${poissonsRatio} ${poissonsRatio}

fix m3 all property/global coefficientRestitution peratomtypepair 3
&   ${coefficientRestitution} ${coefficientRestitution}
${coefficientRestitution} &
    ${coefficientRestitution} ${coefficientRestitution}
${coefficientRestitution} &
    ${coefficientRestitution} ${coefficientRestitution}
${coefficientRestitution}

fix m4 all property/global coefficientFriction peratomtypepair 3 &
                  ${pp11Friction} ${pp12Friction} ${pw13Friction} &
                  ${pp12Friction} ${pp22Friction} ${pw23Friction} &
                  ${pw13Friction} ${pw23Friction} ${ww33Friction}

fix m5 all property/global coefficientRollingFriction
peratomtypepair 3 &
                  ${pp11RollingFriction} ${pp12RollingFriction}
${pw13RollingFriction} &
                  ${pp12RollingFriction} ${pp22RollingFriction}
${pw23RollingFriction} &
                  ${pw13RollingFriction} ${pw23RollingFriction}
${ww33RollingFriction}
```

Followed by instructions for loading the CAD files containing the structure of the system:

```
# Import mesh from cad
fix cad1 all mesh/surface file meshes/Text_geometry.stl type 3 scale 1

# Use the imported mesh as granular wall
fix geometry all wall/gran model hertz tangential history
rolling_friction epsd2 mesh n_meshes 1 meshes cad1

# Create stopper for funnel
fix stopper all wall/gran model hertz tangential history
rolling_friction epsd2 primitive type 3 zplane -0.086403
```

And by the instructions for inserting the particles, which indicates the type of particle to be inserted into the system and defines the surface through which the particles are inserted with a random and discrete particle size distribution.

```
# Particles insertion
fix pts1 all particletemplate/sphere 15485863 atom_type 1 density
constant ${density} radius constant ${radius1}
fix pts2 all particletemplate/sphere 11887    atom_type 2 density
constant ${density} radius constant ${radius2}
fix pdd all particledistribution/discrete 15485867 ${nradii} pts1
${frac1} pts2 ${frac2}
region factory cylinder z 0 0 ${rsilo} ${rsilo} 0.3 units box

fix ins all insert/rate/region seed 32452843 distributiontemplate pdd
&
      mass ${massP} particlerate 500000 insert_every 200 &
      overlapcheck yes vel constant 0. 0. -1.0 region factory ntry_mc
10000
```

Finally, the physical model is defined, for these simulations the Hertzian model without cohesion was chosen, indicated by epsd2:

```
# Define the physics
pair_style gran model hertz tangential history rolling_friction epsd2
#Hertzian without cohesion
pair_coeff * *
```

In this section, *groups* have also been defined; this setting allow to identify and distinguish particles within the system based on size. By indicating coarse particles with the number 1 and fine particles with the number 2, it was possible to obtain detailed information about the system in terms of position, velocity and angular velocity based on the type of particle distinctly.

```
# Define the groups
group large type 1
group small type 2
```

Next, the detailed settings are written. Commands such as the integrator (set to nve/sphere unless multispherical particles are used), gravity (to indicate that the material is free falling), and the time step are entered here.

```
### DETAILED SETTINGS

# Integrator
fix integrate all nve/sphere

# Gravity
fix grav all gravity 9.81 vector 0.0 0.0 -1.0

# Time step
timestep ${deltaT}

# VORONOI
compute     voro all voronoi/atom
```

Note the insertion of the "*Voronoi*" command; this is an optional command, not settled by default, which allows to create a multifaceted volume (or cell) around each particle present in the system. Each cell, therefore, encloses a particle and shares sides with the cells of neighbouring particles. In this work, it was used in order to determine the porosity of the material as the ratio between the volume occupied by the particle compared to the volume created by the voronoi command.
Information regarding the type of information it is wanted to obtain as output is also included in this section; information both of a thermodynamic nature and the so-called "*dump files*", i.e. the files that collect the output variables that represent the dynamics of the system at each instant of time, therefore particle velocity, position, angular velocity and radius.

```
# Thermodynamic output settings
thermo_style custom step atoms ke cpu
thermo 10000
thermo_modify norm no lost ignore

# Create imaging information
# Inizialize dump file so that it is not empty
run    1
dump dmp all custom/vtk 5000 post/filling_*.vtk id type type x y z ix
iy iz vx vy vz fx fy fz omegax omegay omegaz radius
dump voro all custom 1000 post/dump_*_packing.txt id type x y z
c_voro[1] c_voro[2]
```

Finally, there is the execution part, in which it is indicated to create a restart file (every 50 thousand iterations in this example) which is used as a starting point for the subsequent discharge phase, and the command indicating to proceed with the hopper filling for a maximum of 300 thousand iterations. The filling ends when the silo is loaded with a mass that corresponds to that indicated at the beginning of the script, any further iterations would always return the same result; the important thing is to make sure that the iterations are sufficient to load the entire desired mass.

```
### EXECUTION AND FURTHER SETTINGS

# Create a restart file after filling is complete
restart     50000 binsert_*.restart

# Fill the hopper
run 300000 upto
```

5.2.2 Discharge

As for the filling phase, the structure and most of the information contained remain the same. Only the differences compared to the filling script are reported below.
The command indicating to start the download phase starting from the last file generated during loading is inserted in the initiation part.

```
read_restart binsert_250000.restart
```

Additionally, some variables are introduced here, such as the total number of iterations used for discharging. Also in this case, it is important to calculate the appropriate number in order to

ensure that all the material is discharged. The “time” variable refers to an output file that will be defined later.

```
variable dischargestep equal 3000000
variable finalFillingStep equal 250000
variable time equal (step-${finalFillingStep})*${deltaT}
```

In the setup part, measurement functions have been inserted with the aim of measuring variables such as total mass, total number of particles, discharge flow rate in mass and discharge flow rate in terms of number of particles.
In order to use the measurement functions, first of all the exit hole of the silo was indicated as the discharge surface, then were defined the variables to be calculated in correspondence with that surface.

```
# Measure the massflow through outlet
fix Measurement all massflow/mesh mesh outlet count once
point_at_outlet 0. 0. -1.
variable MassTotal equal f_Measurement[1]
variable NoPTotal equal f_Measurement[2]
variable MassFlowRate equal f_Measurement[3]
variable NoPFlowRate equal f_Measurement[4]
```

In the detailed settings part, a command has been inserted that allows to take into consideration a file, external to the script, which contains instructions for further output data. The external file is called *in.stress* and is described in paragraph §5.2.3.

```
# Include file containing all the compute commands
include in.stress
```

The instructions for generating output data relating to the measurement functions shown above have been defined here.

```
fix output all print 100 "${time} ${MassTotal} ${NoPTotal}
${MassFlowRate} ${NoPFlowRate}" file data/Mass_outlet.dat screen no
```

Finally, in the Execution part has been inserted the command which indicates to end the simulation once the last iteration has been reached, as described in the initialization part.

```
# Fill the hopper
unfix stopper
run ${dischargestep}
```

5.2.3 File in.stress

In.stress is a file external to the script that is recalled by means of a specific command, as exposed previously. This file is composed of three parts, in which specific instructions are defined on how it was decided to organize the output data from the simulator.

The first part recalls the voronoi command, introduced in paragraph §5.2.1. Here the total mass of material present inside the silo is calculated starting from the mass of each particle taken individually; iteration after iteration the mass decreases from the initial value to zero, i.e. until the material is completely discharged. The *reduce* command within the script is used to "reduce" one or more input vectors into a scalar value.
Finally, the simulator is instructed to collect the output data in a specific file (*Mass_inside.dat*) as the total mass of material as a function of time. The output data collected in this file were then used to compare the flow rates with the experimental data, as reported in paragraph §7.2.

```
#VORONOI
compute voro all voronoi/atom

variable pMass atom r^3*4/3*PI*density
compute  totMass all reduce sum v_pMass
variable totMassSilo equal c_totMass

fix massIN all print 100 "${time} ${totMassSilo}" file
data/Mass_inside.dat screen no
```

In the second part the simulator is instructed to calculate the average velocity of all fine and coarse particles distinctly in the three directions and to collect the data in a file called *segregationVel.dat*.

```
# Segregation velocity
compute    velMeanSmallx small reduce ave vx
compute    velMeanLargex large reduce ave vx
compute    velMeanSmally small reduce ave vy
compute    velMeanLargey large reduce ave vy
compute    velMeanSmallz small reduce ave vz
compute    velMeanLargez large reduce ave vz
variable   VarVelSmallX equal c_velMeanSmallx
variable   VarVelLargeX equal c_velMeanLargex
variable   VarVelSmallY equal c_velMeanSmally
variable   VarVelLargeY equal c_velMeanLargey
variable   VarVelSmallZ equal c_velMeanSmallz
variable   VarVelLargeZ equal c_velMeanLargez

fix        printSegregationVel  all print 100 &
           "${time} ${VarVelSmallX} ${VarVelSmallY}
${VarVelSmallZ} ${VarVelLargeX} ${VarVelLargeY}
${VarVelLargeZ}" &
file data/segregationVel.dat title "#SEGREGATION VEL: small_x
small_y small_z large_x large_y large_z" screen no
```

Similarly to the first part, in the third one it is indicated to calculate the mass of particles inside the silo at any time; here, on the other hand, it is specified to distinguish between fine and coarse particles and to collect the data in the *segregationMass.dat* file.
Distinguishing the mass based on the type of particle allowed to calculate at any instant the mass fraction of fine particles as a function of the total mass discharged and to compare the results with the experimental data, as shown in paragraph §7.3.

```
# Segregation Mass
compute    massSmall small reduce sum v_pMass
compute    massLarge large reduce sum v_pMass
variable   VarMassSmall equal c_massSmall
variable   VarMassLarge equal c_massLarge

fix             printSegregationM  all print 100 &
           "${time} ${VarMassSmall} ${VarMassLarge}" &
           file data/segregationMass.dat title "#MASS: small
large" screen no
```

Chapter 6

DEM calibration

In chapter §5, as an example, the scripts used for one of the simulations carried out for this study have been reported and commented on. The parameters used and the entire structure of the scripts, on the other hand, are the result of work that took a long time, in order to identify the numerical values that best represented the physical phenomenon to be simulated.
In other words, the macroscopic material behavior needs to be replicated by DEM model, hence the microscopic DEM parameters are to be chosen in such a way that the macroscopic behaviour of the material in the simulation is the same as that in reality.

6.1 Bulk material properties and DEM parameters

The necessary DEM parameters are: Young modulus, Poisson's ratio, coefficient of restitution, coefficient of friction and coefficient of rolling friction. To calibrate DEM simulation to the experimental data, some preliminary simulations were carried out using a mono-component system. Hence, the silo was filled with equal-sized particles with a diameter equal to 3.68 mm. It was chosen to simulate a single-component system using the larger diameter among those used for mixtures in order to reduce the computational time of the simulations.

6.2 Young modulus, Poisson's ratio and coefficient of restitution

The Young modulus, Poisson's ratio and the coefficient of restitution primarily influence the elastic and viscoelastic damping constant for normal and tangential contacts. These constants weakly affect the porosity of the system but especially the viscoelastic damping constant regulates the energy dissipation within the granular material.

In the initial analysis, however, it was decided not to conduct parametric simulations by varying these parameters, but they were kept constant in all simulations. The parameters used are listed in the table 6.1.

Young modulus [MPa]	Poisson's ratio [-]	Coefficient of restitution [-]
$2.5 \cdot 10^7$	0.25	0.5

Table 6.1 – *Young modulus, Poisson's ratio and coefficient of restitution used for all the simulations.*

6.3 Sliding friction coefficient

The sliding friction coefficient is a key parameter that influences both porosity and bulk density, as well as energy dissipation and the flow of the granular material itself in terms of shear interlocking and bulk friction. For this reason, we decided to perform parametric simulations changing it to calibrate the simulations.

As a first approach to verify that the coefficient of sliding friction imposed on the simulation led to results consistent with the experiments, was attempted to calculate the porosity of the granular bed. If the porosity obtained with DEM simulations had been in agreement with the experimental data, it would have been confirmed that the parameters were correct.

To calculate the porosity, an optional additional command of the simulator called Voronoi was used. This command works by implementing a cell with polyhedral faces around each particle. The result is a 3D mesh network that includes the entire volume of the filling. Using Voronoi it is possible to obtain output data which is collected in a specific file. These data were then used to calculate the porosity of the system using the formula:

$$Porosity = 1 - \frac{V}{V_{voro}} \tag{6.1}$$

Where V is the volume of particles and V_{voro} is the volume of cells that compose the system. Hence, for every particle filled in the silo, it was possible to calculate the individual porosity. A mean value of porosity, obtained averaging all the individual porosity, was calculated at the end of the filling process in a static condition (i.e., the mean porosity was calculated at the last time of the filling simulation).

It should be considered that inside the bed of particles the porosity, as well as the density, does not remain constant along the entire height of the filling (Schulze, 2008), which is why to obtain a value comparable with the experimental data was used the mean.
Initially, it was observed that the porosity value obtained was very close to 1, which would suggest that the volume of voids is almost equal to the volume of the system, that is conceptually an error. To explain this result, it was thought that presumably the Voronoi command, also taking into consideration the region of particles exposed to the free surface, incorrectly estimated a much larger vacuum region than that is actually considered for the calculation.
To overcome this problem, it was decided to modify the way with which the porosity was calculated, defining a parallelepiped-shaped region within the volume of the particle system and calculating the porosity exclusively in that region. In this way, both the error due to the surface region and the possible error due to the regions closest to the walls of the container would have been avoided.

The porosity can be interpreted as a representation of how the particles pack together during the filling phase, which in turn depends on the sliding friction value between the particles, which is one of the parameters that are given as input to the simulator. To understand how the sliding friction coefficient influence the bulk porosity a series of simulations were carried out, varying the particle-particle sliding friction coefficient from 0.1 to 0.7, and to calculate the mean porosity trend as a function of friction.
In Figure 6.1 it is possible to observe the trend of porosity as a function of the sliding friction coefficient. Table 6.2 shows the porosity values calculated by varying the particle-particle sliding friction coefficient (pp).
The bulk porosity increases with the increase of the sliding friction coefficient; this because increasing the friction coefficient between the particles the packing capacity decreases, as the particles were unable to slide relative to each other. Consequently, less packing would have translated into greater empty space between the particles and therefore a lower density and higher porosity.
The DEM bulk porosity was compared with the bulk porosity calculated experimentally as described in the paragraph §3.2.2.

Sliding Friction [-]	Porosity [-]
0.1	0.4404
0.2	0.4477
0.3	0.4527
0.4	0.4565
0.5	0.4589
0.6	0.4610
0.7	0.4617

Table 6.2 – *Bulk porosity calculated as function of sliding friction coefficient.*

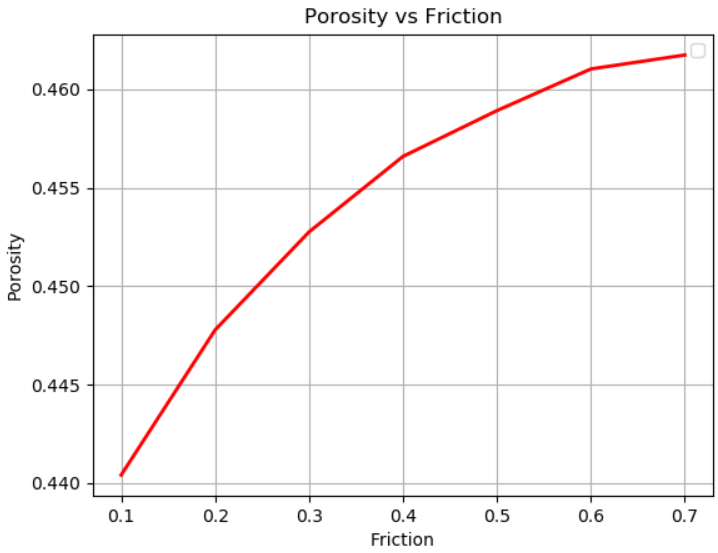

Figure 6.1 – *Bulk porosity vs sliding friction coefficient.*

6.4 Rolling friction coefficient

A further problem arises from the fact that experimentally we observed a discharge in the funnel flow regime, as previously mentioned.

To obtain also with simulations this type of flow, it was decided to consider the contribution of rolling friction. The rolling friction, in combination with the sliding friction, has a strong influence on the bulk friction behaviour (McGlinchey, 2023).

After introducing the rolling friction coefficient, it was possible to observe that all the simulations presented, during unloading, the characteristic V-shape structure at the top of the filling. This shape is distinctive in silos that discharge in funnel flow and clearly shows that the

material follows a preferential path in the central part. Figure 6.2 shows a picture obtained using the Paraview visualization software.

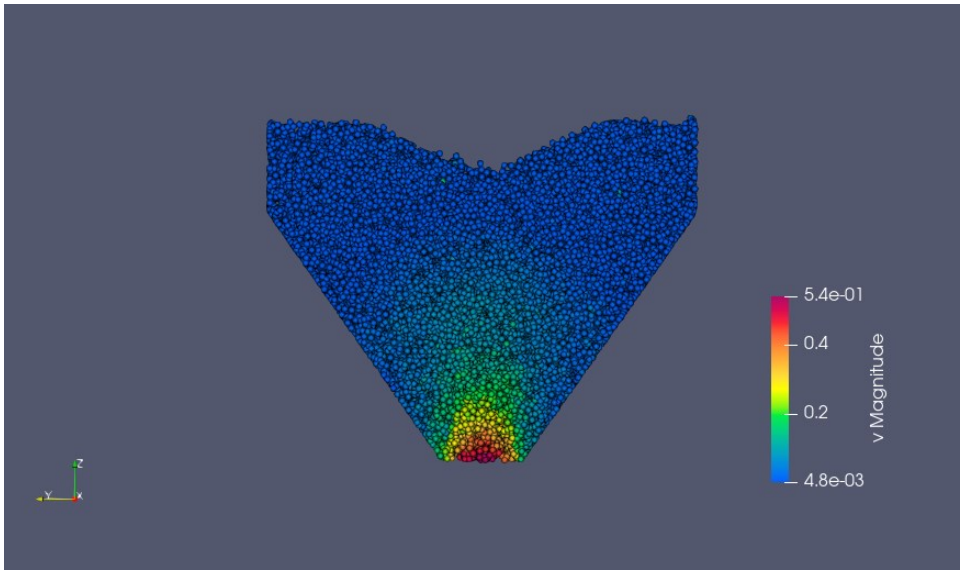

Figure 6.2 – *Funnel flow characteristic V-shape structure of DR=3 (65f-35c) simulation.*

6.4.1 Rolling friction models

To take rolling friction into consideration it is necessary to modify the simulator script by adding the rolling friction variable and modify the physics of the simulation by inserting an appropriate contact model. Two types of rolling friction models were considered: Epsd2 and Cdt.
The simulator provides a series of possible models, the one chosen is called "Epsd2" an acronym which stands for "*Alternative elastic-plastic spring-dashpot model*".

6.4.2 Particle-particle rolling friction coefficient

The expectation was that this further contribution could also lead to an improvement in the porosity calculation described previously. In reality, it was observed that acting solely on the particle-particle rolling friction coefficient does not result in an increase in the static bed porosity, as can be seen from Table 6.3.

	Sliding Friction	Rolling Friction	Porosity
TEST A	0.7	0.8	0.4531
TEST B	0.8	0.9	0.4569
TEST C	0.9	0.9	0.4607

Table 6.3 - *Values of sliding friction and rolling friction used in the simulations in the Epsd2 model.*

6.4.3. Particle-particle and wall-particle rolling friction coefficients

At this point several simulations were carried out by varying the values of the friction coefficients (both sliding friction and rolling friction). To confirm that the procedure and the results obtained had useful feedback, the trends in mass discharged as a function of time obtained from the simulations were compared with that obtained experimentally (see paragraph §3.2.1.

To better represent the friction between the various materials of the system, it was chosen to also take into account the contact between particles and the silo wall. To do this it was necessary to define two 2x2 matrices of variables in the script (one for sliding and one for rolling) that reported the friction coefficients. The matrices are both symmetric, so the elements off the diagonal represent the particle-wall pair (pw and wp), while the elements on the diagonal represent the particle-particle (pp) and wall-wall (ww) pairs. This last element does not have a real physical meaning but was nevertheless necessary for completeness when defining the variables.

The first three tests were conducted by varying the sliding and rolling friction coefficients for both the particle-particle contact and the particle-wall contact (Test 1, 2 and 3), the numerical values are shown in Table 6.4. Note that in this phase the rolling friction coefficient has been set the same for both types of contact.

	Model	Sliding Friction (Pp)	Sliding Friction (Pw)	Rolling Friction (Pp)	Rolling Friction (Pw)
TEST 1	Epsd2	0.8	0.4	0.7	0.7
TEST 2	Epsd2	0.7	0.4	0.6	0.6
TEST 3	Cdt	0.8	0.4	0.8	0.8

Table 6.4 - *Values of sliding and rolling friction used in test 1, 2 and 3.*

Note that the Test was done with the model named Cdt and described above. It was used at this first stage as an alternative to Epsd2; but, as will be seen later from the plots shown in Figure 6.3, it only served to confirm that the elastic-plastic model better represents the real behavior of the system.

Note that most of the plots that will be shown from now on in this chapter have the simulator discharging line interrupted at half of the process. This was done because, for the purposes of the parametric analysis, what matters is the slope of the line. To significantly reduce the simulation time, therefore, only a sufficient number of iterations was considered to visualize the slope of the line with respect to the line of the experimental data. Since it is not necessary to complete each simulation, this procedure was chosen to optimize the time available for the search for parameters.

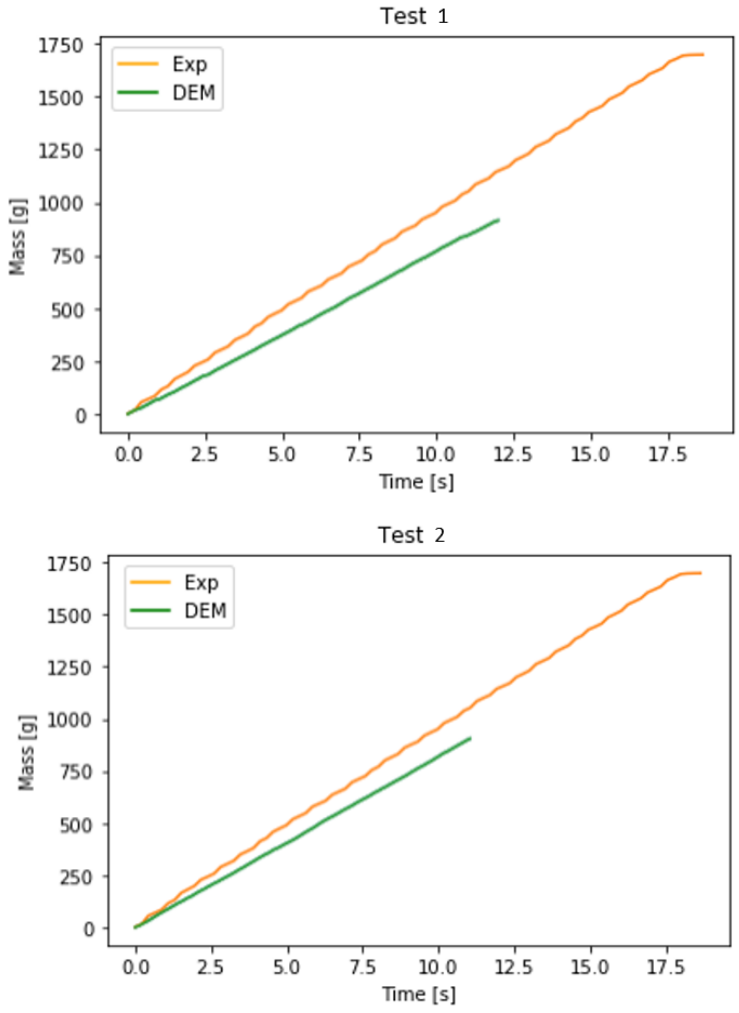

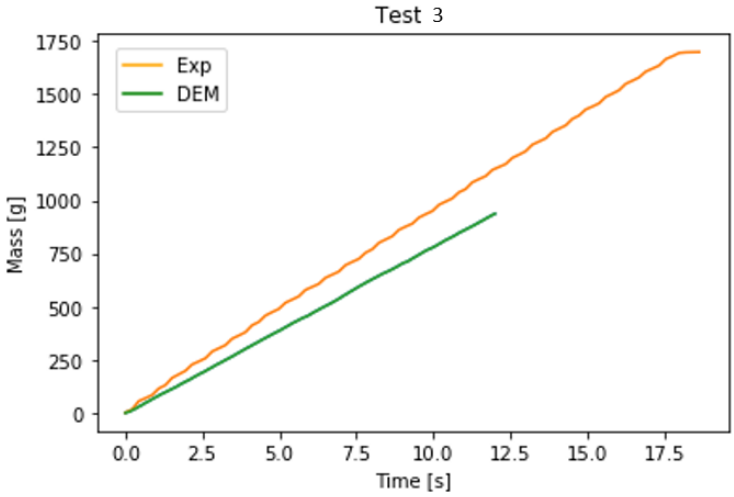

Figure 6.3 – *Mass vs time results of test 1, 2 and 3.*

Looking at the plots, it can be noted that in all three simulations the discharge line has a lower slope than the line of the experimental data, indicating that, with these parameters the systems discharge the material more slowly than in reality. Comparing them with each other, Test 2 better represents the experimental data having lower friction coefficients than the other two cases. In particular, it is concluded that to get closer it is necessary to further reduce the coefficients.

Four further simulations were conducted (Tests 4, 5, 6 and 7) using the parameters of the second test as a starting point. In these simulations, only one parameter was reduced at a time (in red in Table 6.5) compared to Test 2, to investigate which contribution had the greatest influence and brought the simulation results closer to the experimental data; the other values were left unchanged.

	Model	Sliding Friction (Pp)	Sliding Friction (Pw)	Rolling Friction (Pp)	Rolling Friction (Pw)
TEST 2	Epsd2	0.7	0.4	0.6	0.6
TEST 4	Epsd2	0.7	0.4	0.6	0.4
TEST 5	Epsd2	0.7	0.4	0.4	0.6
TEST 6	Epsd2	0.7	0.2	0.6	0.6
TEST 7	Epsd2	0.5	0.4	0.6	0.6

Table 6.5 - *Values of sliding and rolling friction used in test 2, 4, 5, 6 and 7.*

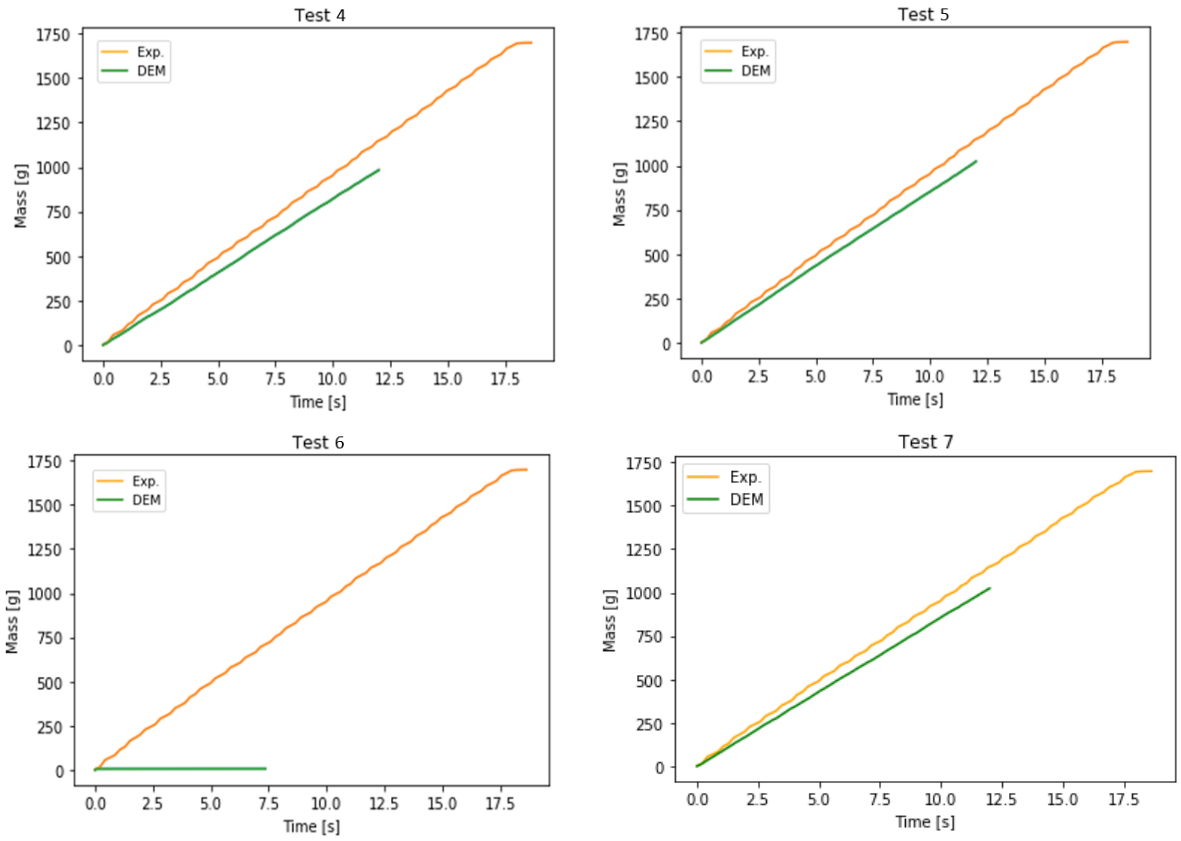

Figure 6.4 – *Mass vs time results of test 4, 5, 6 and 7.*

Looking at the plots in Figure 6.4, Tests 5 and 7 are closer to the experimental data than the other two, indicating that it is precisely the particle-particle contact that plays a crucial role.

Test 6 led to an unexpected result: the parameters used led to blocking of the material near the exit. The explanation given is that after very few iterations, the material developed a stable arc structure.

Confirmation of this block came in various forms:

1) The number of particles present in the silo as a function of the iterations almost from the beginning remained constant until the end of the simulation.
2) Looking at the trend of the mass discharged over time shows that the mass in the silo remains constant immediately.
3) For visual confirmation, the *Paraview* graphic representation software was used in which the formation of an arch near the exit hole of the silo was evident.

This result was particularly unexpected as this phenomenon manifests itself more when using materials that tend to give cohesion, which derives from interparticle forces given by the

properties of the material or from any agglomerates that are added to the system, but it is obvious that this is not the case.

The results of the various simulations have been unsatisfactory up to this point. Having identified the particle-particle contact in terms of sliding and rolling friction as more influential than the others, two further simulations were conducted (Tests 8 and 9) in which both the sliding and rolling friction contributions were reduced; numerical values are shown in Table 6.6.

	Model	Sliding Friction (Pp)	Sliding Friction (Pw)	Rolling Friction (Pp)	Rolling Friction (Pw)
TEST 8	Epsd2	0.4	0.4	0.3	0.6
TEST 9	Epsd2	0.3	0.4	0.2	0.6

Table 6.6 - *Values of sliding and rolling friction used in test 8 and 9.*

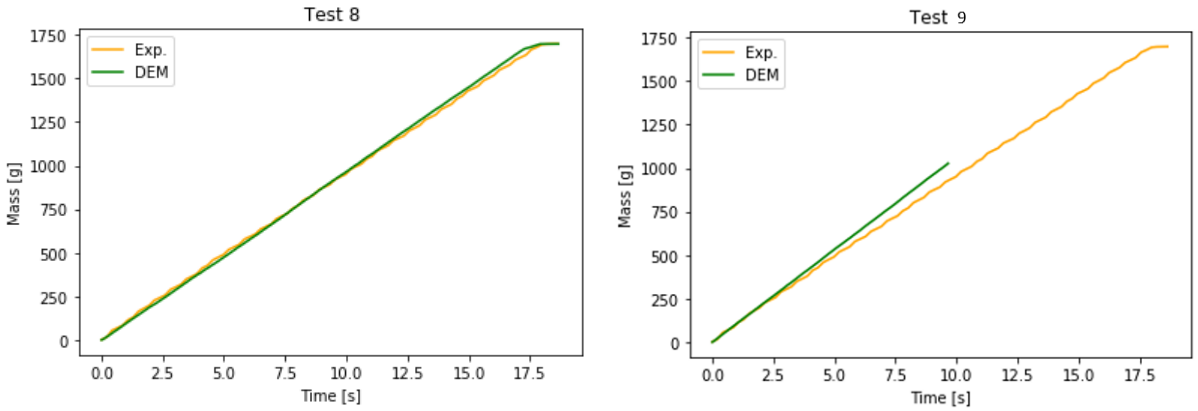

Figure 6.5 – *Mass vs time results of test 8 and 9.*

As can be seen from the plots in Figure 6.5, Test 8 perfectly represents the experimental data, while Test 9, the coefficients were decreased excessively, leading to a discharging line with a slope greater than that of the experimental data, i.e. a system that discharge faster than the real system does.

The parameters of Test 8 were, therefore, taken as the basis for the subsequent simulations.

6.5 DEM parameters for binary mixtures

The next step was to consider systems of binary mixtures. In order to obtain parameters that were suitable for all the mixtures under examination (10f-90c, 30f-70c, 50f-50c and 65f-35c) it was decided to work with the 30f-70c mixture. In fact, the 10f-90c mixture was considered not representative enough as it is too close to the composition used for the tests described previously (0f-100c).

Then, using the parameters of Test 8 (the best so far), a simulation was conducted by inserting into the simulator the variables describing the mole fraction, 0.3 for fine particles and 0.7 for coarse particles.

As a further improvement to the simulation, the groups have been defined here, as shown in the script in chapter §5. By distinguishing fine particles from coarse ones, it was possible to obtain more precise output data in terms of position, velocity and angular velocity based on particle type distinctly.

To do this it was necessary to expand the two matrices reporting the friction coefficients, from 2x2 to 3x3. In this way were also defined the friction coefficients relating to the coarse particle-fine particle pairs (pp12 and pp21), coarse particle-wall (pw13 and wp31) and fine particle-wall (pw23 and wp32).

In this phase, seven simulations were conducted (Tests 10, 11, 12, 13, 14, 15 and 16). The parameters used are shown in Table 6.7, where the parameters modified respect to Test 8 are indicated in red.

	Sliding Friction			Rolling Friction		
TEST 10	pp11=0.4	pp12=0.4	pw13=0.4	pp11=0.3	pp12=0.3	pw13=0.6
	pp21=0.4	pp22=0.4	pw23=0.4	pp21=0.3	pp22=0.3	pw23=0.6
	pp31=0.4	pp32=0.4	ww33=0.4	pp31=0.6	pp32=0.6	ww33=0.6
TEST 11	pp11=0.4	pp12=0.4	pw13=0.4	pp11=0.3	pp12=0.5	pw13=0.6
	pp21=0.4	pp22=0.4	pw23=0.4	pp21=0.5	pp22=0.5	pw23=0.6
	pp31=0.4	pp32=0.4	ww33=0.4	pp31=0.6	pp32=0.6	ww33=0.6
TEST 12	pp11=0.4	pp12=0.4	pw13=0.4	pp11=0.3	pp12=0.3	pw13=0.6
	pp21=0.4	pp22=0.4	pw23=0.4	pp21=0.3	pp22=0.3	pw23=0.8
	pp31=0.4	pp32=0.4	ww33=0.4	pp31=0.6	pp32=0.8	ww33=0.6
TEST 13	pp11=0.4	pp12=0.4	pw13=0.4	pp11=0.3	pp12=0.5	pw13=0.6
	pp21=0.4	pp22=0.4	pw23=0.4	pp21=0.5	pp22=0.5	pw23=0.8
	pp31=0.4	pp32=0.4	ww33=0.4	pp31=0.6	pp32=0.8	ww33=0.6
TEST 14	pp11=0.4	pp12=0.4	pw13=0.4	pp11=0.3	pp12=0.1	pw13=0.6
	pp21=0.4	pp22=0.4	pw23=0.4	pp21=0.1	pp22=0.1	pw23=0.8
	pp31=0.4	pp32=0.4	ww33=0.4	pp31=0.6	pp32=0.8	ww33=0.6
TEST 15	pp11=0.4	pp12=0.4	pw13=0.4	pp11=0.3	pp12=0.7	pw13=0.6
	pp21=0.4	pp22=0.4	pw23=0.4	pp21=0.7	pp22=0.7	pw23=0.9
	pp31=0.4	pp32=0.4	ww33=0.4	pp31=0.6	pp32=0.9	ww33=0.6
TEST 16	pp11=0.6	pp12=0.6	pw13=0.6	pp11=0.3	pp12=0.7	pw13=0.6
	pp21=0.6	pp22=0.6	pw23=0.6	pp21=0.7	pp22=0.7	pw23=0.9
	pp31=0.6	pp32=0.6	ww33=0.6	pp31=0.6	pp32=0.9	ww33=0.6

Table 6.7 *-Values of sliding and rolling friction used in test 10, 11, 12, 13, 14, 15 and 16.*

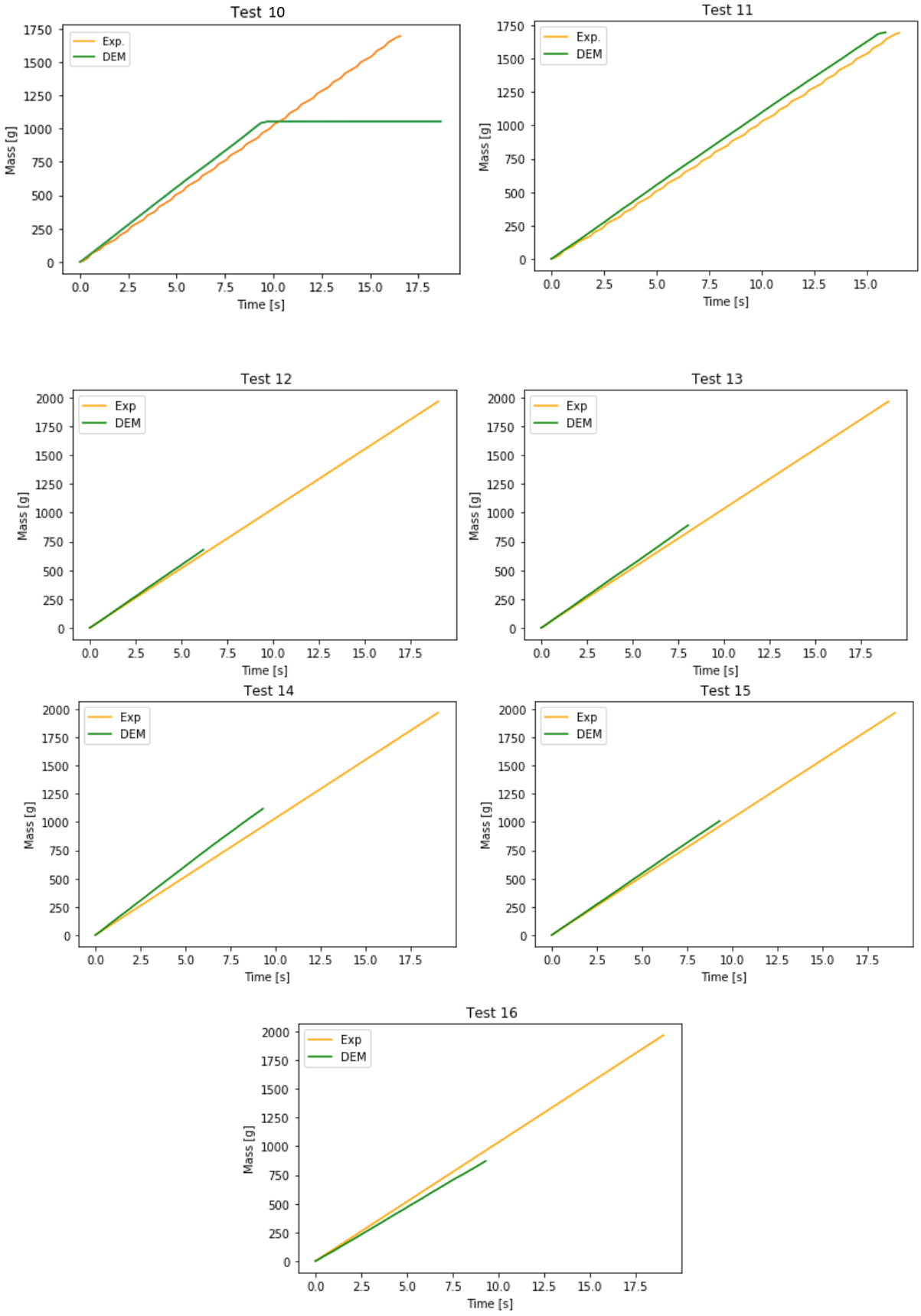

Figure 6.6 – *Mass vs time results of test 10, 11, 12, 13, 14, 15 and 16.*

In Test 10 the same parameters as Test 8 were used. However, from the plots we can see that once the percentage of fine particles has increased, these parameters no longer represent the experimental data adequately; furthermore, we note that once reaching just over half the simulation the mass remains constant until the end of the process, which suggests that the material is blocked near the exit due to the formation of a stable arc structure.
In Tests 11, 12, 13, 14 and 15, therefore, we attempted to vary the rolling friction coefficients in order to understand which contact was most influent. From the results obtained it was understood that to get closer to the experimental data the coefficients had to be increased (Tests 11, 12 and 13), both as regards the particle-particle pair and the particle-wall pair. While decreasing the coefficients leads to the opposite result, as can be seen from Test 14.
In particular, it should be noted that we focused on the modifications of the coefficients of the pairs that include the fine particles (type 2). This is because it is right the percentage of fines that has been increased compared to the single-component system described previously, so it was believed that the coefficients relating to the fines were responsible for the deviation from the experimental data.
Note that Test 16, in which the coefficients relating to sliding friction were also increased, led to a line with a lower slope than that of the experimental data; therefore, to a system that downloads more slowly than it actually does.
Test 15, among all, was the one that gave the best results, as it approached the experimental data with a deviation that was considered acceptable.

Having identified the parameters considered acceptable for the continuation of the investigation, two further simulations were carried out in which the percentage compositions by weight were varied (Test 17 with 10% fine - 90% coarse and Test 18 with 50% fine - 50% coarse)
The results of Tests 17 and 18 are shown in Figure 6.7.

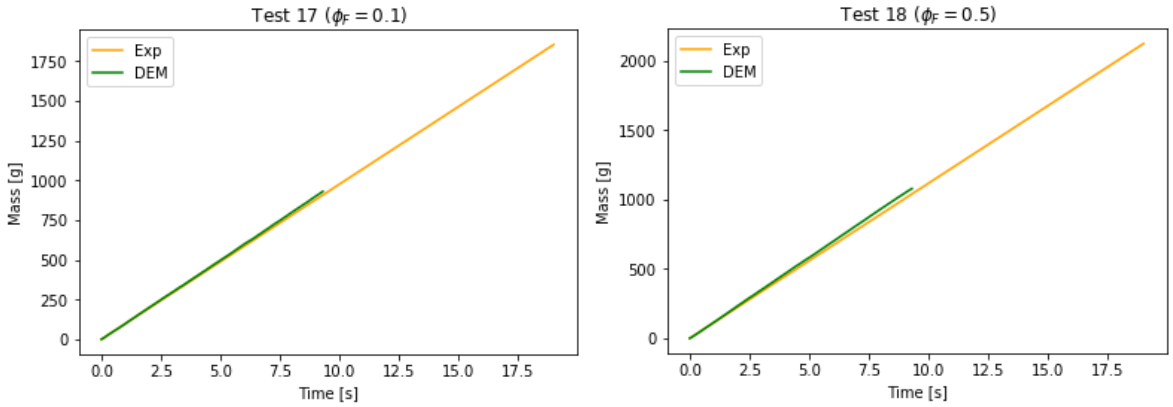

Figure 6.7 – *Mass vs time results of test 17 and 18.*

Both graphs show that the parameters found during the analysis are sufficiently adequate to represent the experimental data.

6.6 Conclusions

What has been presented in this chapter is the process that led to identifying the parameters to be used as input to the simulations. In particular, we focused on the sliding and rolling friction coefficients, which were considered the most influential parameters. Other parameters that could have been concentrated on are the Young's modulus, the coefficient of restitution and the Poisson's ratio, which were considered of secondary interest for the purpose of this study and kept constant for all the simulations carried out. Certainly, an in-depth study of the influence that these parameters have on the representation of experimental data will be able to lead to even more accurate results.

Chapter 7

Results

Chapter §3 describes the work carried out in the laboratory regarding the study of percolation mechanisms. As mentioned, this thesis aims to replicate the experimental work through the LIGGGHTS simulator using the DEM approach. This chapter will present the main simulations used for the purposes of this investigation and the results obtained.

7.1 The simulations

Once the optimal parameters to represent the binary mixture under examination had been identified, as explained in Chapter §6, the eight main simulations were conducted.

All simulations consist of a filling phase and a discharging phase. They were divided into two series which differ in diameter ratio, DR = 3 and DR = 2.16, and for each series four simulations were conducted by varying the weight percentage of fines present in the mixture: 10%, 30%, 50% and 65%.

	DR	Composition
A	2.16	10% fine – 90% coarse
B	2.16	30% fine – 70% coarse
C	2.16	50% fine – 50% coarse
D	2.16	65% fine – 35% coarse
E	3	10% fine – 90% coarse
F	3	30% fine – 70% coarse
G	3	50% fine – 50% coarse
H	3	65% fine – 35% coarse

Table 7.1 – *Diameter ratio and composition of the eight main simulations.*

Table 7.2 reports the characteristics of the experiments and the respective simulations, in terms of mass of the experimental filling, mass of the DEM filling and initial mass of fine and coarse particles.

	Experimental filling mass [g]	DEM filling mass [g]	DEM initial fine particles mass [g]	DEM Initial coarse particles mass [g]
A	2274	2279	227	2052
B	2244	2244	673	1570
C	2276	2274	1137	1137
D	2269	2269	1475	794
E	2271.69	2277	227	2051
F	2285.33	2281	684	1597
G	2278.27	2280	1140	1140
H	2462	2451	1594	857

Table 7.2 *–Experimental and DEM filling mass and initial fine and coarse particles mass of the eight main simulations.*

Note that the experimental and DEM filling mass have slightly different values, although the correct (experimental) mass was initially set in the simulator in each case. This is probably due to the fact that the simulator, based on the input data of particle size, density and mole fraction, calculated a different number of particles (fine and coarse) with respect it actually was with the imposed composition. The simulated particles, in fact, have the "limit" of being perfectly spherical and with constant density all over the volume, unlike what happens in reality. Furthermore, it should be considered that sieving cuts were used in the experiments to represent the classes to which the particles belong. So, the dimensions of the particles are included within a size range (3.36-4 mm for coarse particles, 1-1.41 mm and 1.41-2 mm for fine ones), while in the simulations all the coarse particles have a diameter equal to the set one (3.68 mm) and the same goes for the fine particles (1.2 mm and 1.7 mm). Finally, it should be considered that problems such as breaking or chipping particles can arise in the laboratory, leading to inevitable measurement errors.

7.2 Mass flow rate

Here the plots regarding the comparison between the discharge flow rates of the simulations compared to the experimental data are shown in Figure 7.1. The procedure is the same as presented in chapter §6 for the tests carried out during the parametric analysis.

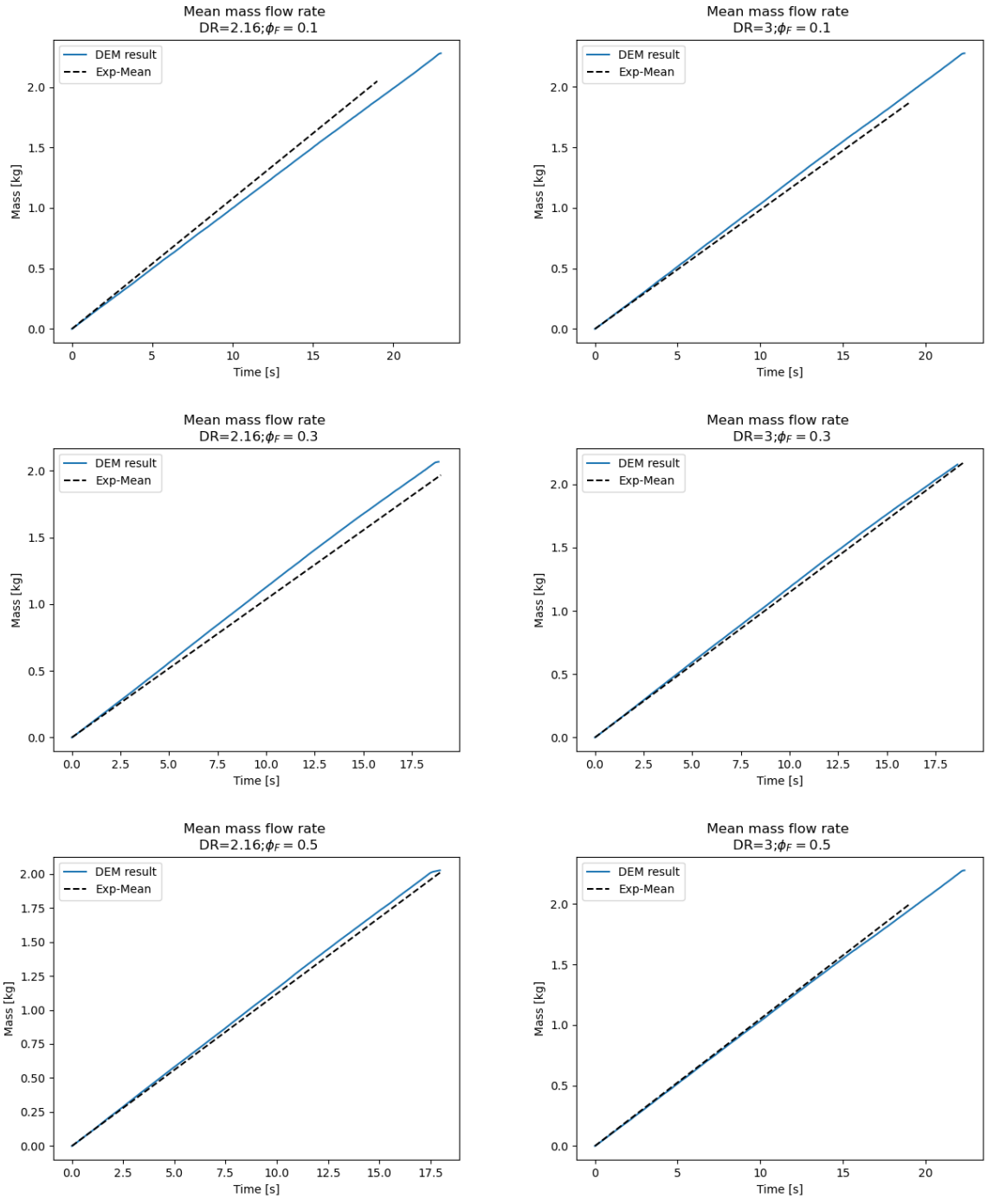

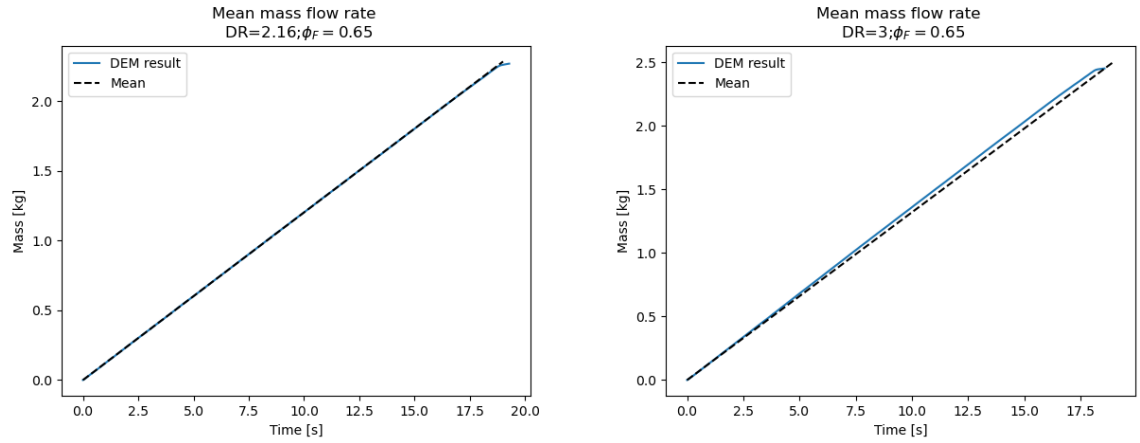

Figure 7.1 – *Comparison of mean mass flow rate between experimental data and DEM results.*

From plots, we can see that most of the results of the simulations coincide almost perfectly with the flow rates of the experiments. Except for simulations DR = 2.16 with compositions 10f-90c and 30f-70c.

This confirms that the parameters found with the parametric analysis adequately represent the mixture.

This excellent result demonstrates that the DEM simulation method confirms itself as an extremely effective tool for the simulation of granular systems like this, representing the dynamics of materials better than expected.

7.3 Mass of fine fraction discharged

For the study of the segregation mechanisms in the binary mixtures discharged from the silo and for the comparison with the experimental data, the same approach used by Santomaso and Volpato, shown in chapter §3, was considered. For this reason, the trend of the mass fraction ϕ_F normalized by the average mass fraction of the initial filling $\phi_{F,0}$ was studied compared to the cumulative overall mass discharged normalized by the initial total mass loaded into the silo.

Figure 7.2 shows the plots of the results obtained for the various simulations.

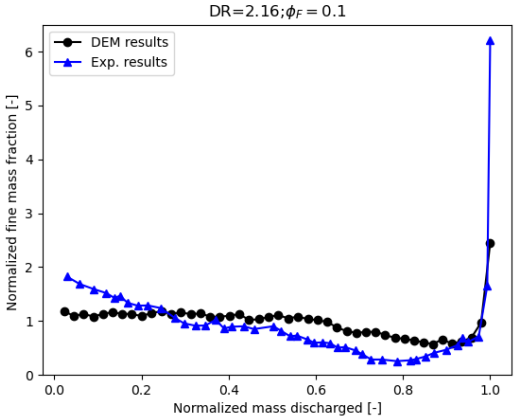
DR=2.16;$\phi_F = 0.1$
DEM results
Exp. results
Normalized fine mass fraction [-]
Normalized mass discharged [-]

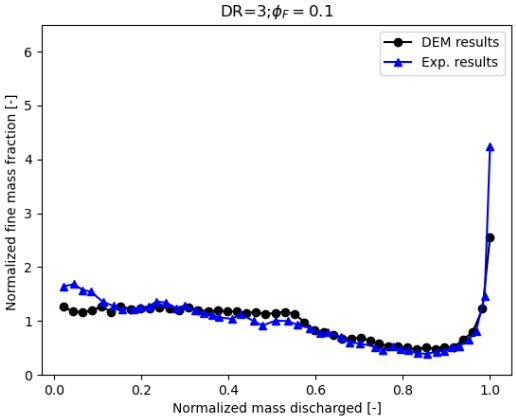
DR=3;$\phi_F = 0.1$
DEM results
Exp. results
Normalized fine mass fraction [-]
Normalized mass discharged [-]

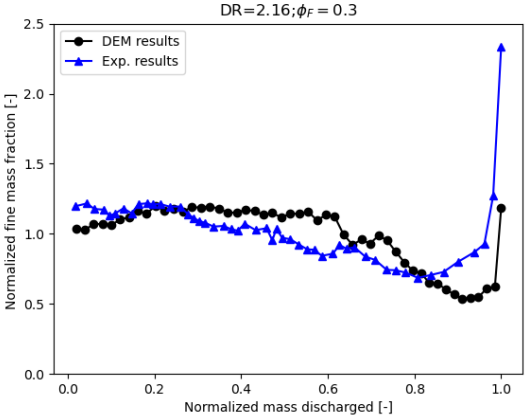
DR=2.16;$\phi_F = 0.3$
DEM results
Exp. results
Normalized fine mass fraction [-]
Normalized mass discharged [-]

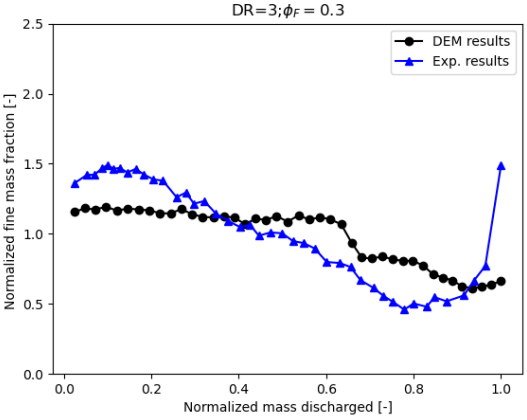
DR=3;$\phi_F = 0.3$
DEM results
Exp. results
Normalized fine mass fraction [-]
Normalized mass discharged [-]

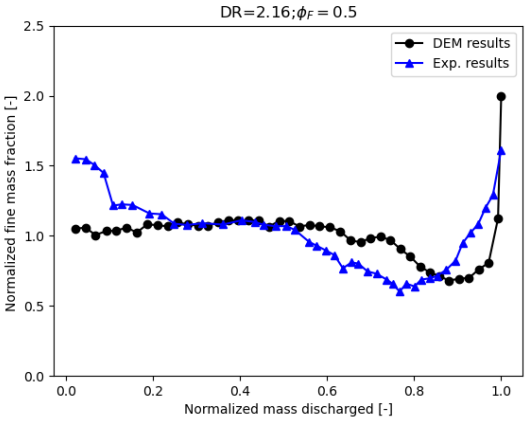
DR=2.16;$\phi_F = 0.5$
DEM results
Exp. results
Normalized fine mass fraction [-]
Normalized mass discharged [-]

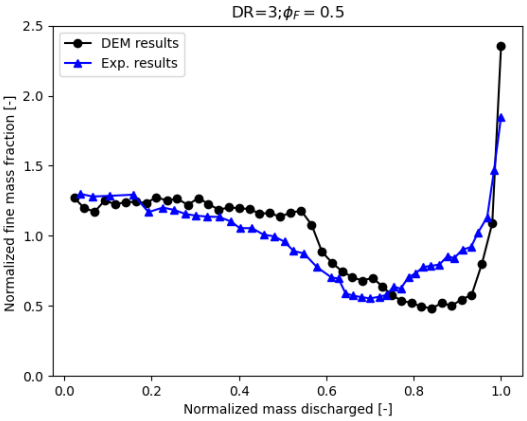
DR=3;$\phi_F = 0.5$
DEM results
Exp. results
Normalized fine mass fraction [-]
Normalized mass discharged [-]

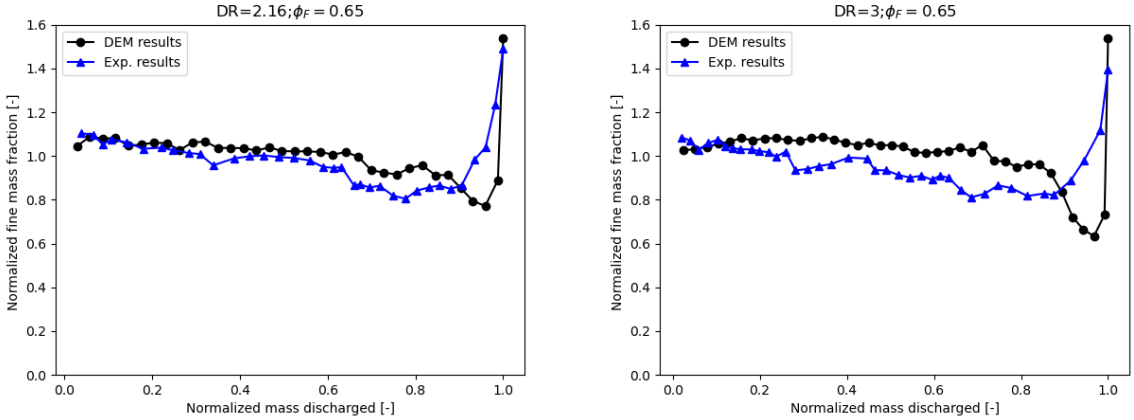

Figure 7.2 - *Comparison normalized fine mass fraction vs normalized mass discharged between experimental data and DEM results*

From the plots it is possible to see that the trend of the mass fraction of fines compared to the total mass discharged is the same as the experimental data; however, in some cases it does not coincide perfectly. It is noted that in all the plots the three regions described in paragraph §3.2.2 are present: one region for low values of discharged mass in which the fraction of fine particles is greater than 1 (indicating that there is segregation due to percolation inside the silo), one central region in which the fines fraction drops to values less than 1 (which indicates retention of fine particles inside the silo, so most of the material discharged is composed of coarse particles), finally one region corresponding to the end of the process, i.e. for high values of mass discharged, in which a peak in the fraction of fine particles is noted (indicating that at the end of the process only the fine particles are discharged).

Speaking about the comparison with the experimental data, it can be noted that for $\phi_F = 0.1$ the curves coincide almost perfectly, both for the case DR = 2.16 and DR = 3; while increasing the percentage of fines the differences become more evident.

Note that, in all cases, for low values of discharged mass the simulation curves start from values slightly lower and closer to 1 than the experimental data. This indicates that numeric particle generation comes closer to the desired random mixture than laboratory-made mixtures. Furthermore, it can be deduced that segregation mechanisms presumably occurred due to the movement of the mixture during the filling phase in the laboratory. This type of error, unwanted and inevitable, is totally avoided with the use of a simulator; on the other hand, it should be remembered that the results of a simulation are subject to errors due to the limitations of the simulator itself. For this reason, it is always necessary to check its efficiency.

All plots show for high values of mass discharged a characteristic curve, which indicates a decrease of the normalized fraction of fines until the minimum is reached, followed by a rapid increase up to values greater than 1 (transition between second and third region, described above); it can be noted that in simulations with $\phi_F \geq 0.5$ this curve is slightly shifted to the right compared to the experimental data. This shows that in the simulations there is a retention of the granular material that lasts until almost the end of the process. This phenomenon is also confirmed by the fact that the curves rise reaching higher values, which means that at the end of the process a greater quantity of fine granular material is discharged in the simulations compared to what happens in reality.

Finally, it is observed that, once the initial phase has passed, the curve of the experimental data lies below the curve of the DEM simulations for most of the process. This indicates that greater fine material retention occurs in the experiments compared to the simulations; therefore, more fine material remains trapped inside the silo. It is likely that this occurs due to percolation which allows the movement of small particles towards the walls of the hopper where they remain stationary, to be subsequently discharged only when the hopper is almost completely emptied.

7.4 RMSE and RNMSE

Finally, we have evaluated the performance of the model by calculating the root-mean-square error (RMSE) and the normalized root-mean-square error (NRMSE) for each component of each plot of Figures 7.2:

$$RMSE_i = \sqrt{\frac{\sum_{j=i}^{n}\left(\hat{y}_{i,j} - y_{i,j}\right)^2}{n}} \tag{7.1}$$

$$NRMSE_i = \frac{RMSE_i}{\bar{y}_i} \tag{7.2}$$

where $\hat{y}_{i,j}$ indicates the predicted values, n is the number of data points and $\bar{y}_i$ is the average experimental volume fraction of i. The results are reported in tables 7.3 and 7.4.

ϕ_F	0.1	0.3	0.5	0.65
RMSE	0.66	0.22	0.24	0.10
NRMSE	0.35	0.34	0.18	0.14

Table 7.3 – *RMSE and NRMSE with DR=2.16*

ϕ_F	0.1	0.3	0.5	0.65
RMSE	0.3	0.23	0.27	0.13
NRMSE	0.14	0.4	0.49	0.14

Table 7.4 – *RMSE and NRMSE with DR=3*

Looking at the values, we note that only the simulations with ϕ_F = 0.65 differ from the experimental data by an error less than 15%, while all the others have larger errors, up to a deviation close to or greater than 50%.

The cause of this deviation from the experimental data lies in the geometry of the particles. Rolling friction seems to be able to compensate for the irregular shape only with regard to the silo's discharge flow rate, as can be seen from plots shown in Figure 7.1. However, it is not sufficient to completely reproduce the complexity of the percolation phenomenon, in which it is possible that the geometry of the interparticle porosities plays a crucial role, which is closely related to the shape of the particles themselves that make up the bed.

It is evident that the composition of the mixture and the irregular shape greatly influence the ability of the fine particles to insinuate themselves into the cavities (also irregular in shape) created between the coarse ones. The irregular shape does not make it easier to fall into the cavities, while the simulated (spherical) particles, regardless of friction, are able to fill the voids more easily.

Chapter 8

Conclusions

The aim of this work was to study the phenomenon of segregation from a numerical perspective, using a discrete approach through LIGGGHTS software.
Simulations were therefore conducted to simulate the behavior of a binary granular mixture during discharge from a pilot silo operating in funnel-flow. A preliminary study to calibrate the simulations based on experimental data allowed us to understand that the parameters that have the most influence on the macroscopic dynamics of the system are the coefficients of sliding friction and the coefficient of rolling friction.
The results of DEM simulations regarding segregation were compared with the experimental data provided by the work of Prof. Santomaso and Dr. Volpato, who studied this phenomenon at the ATP Lab in Padua.
The study involved the examination of eight distinct mixtures, where variations were made in the diameter ratio between the two components comprising the mixture and their respective compositions. The simulations yielded qualitative results very similar to the experimental ones, and a strong correlation with the latter was demonstrated by the values of the root mean square error. Discrepancies between the simulation data and the experimental data can be attributed to the fact that the material used in the experiments has an irregular shape, while spherical particles were simulated in the simulations.

Furthermore, this thesis demonstrated that the DEM approach is a powerful tool for simulating granular materials accurately and in detail, with a wide range of potential applications. Its role in science and engineering will continue to grow, as it provides valuable solutions to granular materials challenges in multiple contexts. Future research in this field could further broaden the understanding and capabilities of the DEM approach.

Bibliography

Artega, P., & Tüzün, U. (1990). Flow of binary mixtures of equal-density granules in hoppers size segregation, flowing density and discharge rates. Chemical engineering science, 45(1), 205-223.

Artoni, R., Santomaso, A., & Canu, P. (2009). Simulation of dense granular flows: Dynamics of wall stress in silos. Chemical engineering science, 64(18), 4040-4050.

Bertrand, F., Leclaire, L. A., & Levecque, G. (2004). Numerical models for the mixing of granular materials.

Fan, Y., Schlick, C. P., Umbanhowar, P. B., Ottino, J. M., & Lueptow, R. M. (2014). Modelling size segregation of granular materials: the roles of segregation, advection and diffusion. Journal of fluid mechanics, 741, 252-279.

Bagi, K. (2012). Fundaments of the discrete element method. Lecture notes.

Lacey, P. M. C. (1954). Developments in the theory of particle mixing. Journal of applied chemistry, 4(5), 257-268.

Rhodes, M. (1998). Mixing and segregation. Introduction to particle technology, 223-240.

Rhodes, M. (1998). Storage and Flow of Powders-Hopper Design. Introduction to particle technology, 265-292.

McGlinchey, D. (2023). Simulations in Bulk Solids Handling: Applications of DEM and other Methods.

Nedderman, R. M. (1992). Statics and kinematics of granular materials (Vol. 352). Cambridge: Cambridge University Press.

Cleary, P. W., & Sawley, M. L. (2002). DEM modelling of industrial granular flows: 3D case studies and the effect of particle shape on hopper discharge. Applied Mathematical Modelling, 26(2), 89-111.

Holdich, R. (2020). Fundamentals of particle technology. MidlandIT.

Bertuola, D., Volpato, S., Canu, P., & Santomaso, A. C. (2016). Prediction of segregation in funnel and mass flow discharge. Chemical Engineering Science, 150, 16-25.

Schulze, D. (2021). Powders and bulk solids. Springer International Publishing.

Volpato, S., & Santomaso, A. C. (2017). Modellazione numerica di flussi granulari. Bollettino Panta Rei, 16, 9-14.

Volpato, S., & Santomaso, A. C. (2023). Particle Size Segregation During the Discharge of Binary Mixtures and the Role of Void Saturation. Chemical Engineering Transactions, 100, 145-150.

Luding, S. (2008). Introduction to discrete element methods: basic of contact force models and how to perform the micro-macro transition to continuum theory. European journal of environmental and civil engineering, 12(7-8), 785-826.

Volpato, S. (2013). Studio numerico del flusso e della distribuzione degli sforzi in sili con e senza inserti.

Volpato, S., Artoni, R., & Santomaso, A. C. (2014). Numerical study on the behavior of funnel flow silos with and without inserts through a continuum hydrodynamic approach. *Chemical Engineering Research and Design*, *92*(2), 256-263.

Zhang, Z., Liu, Y., Zheng, B., Sun, P., & Li, R. (2020). Local percolation of a binary particle mixture in a rectangular hopper with inclined bottom during discharging. ACS omega, 5(33), 20773-20783.

Web Sites:

https://www.cfdem.com/media/DEM/docu/Manual.html